Supporting Information

Diversified Lanthanide-Directed Self-Assembly of Tritopic Tetradentate Acylhydrazone Ligand

Ze-Hong Chen, [a,b,d] Hui-Min Cai, [a,b,d] Xiao-Shan Feng, [b,c] Li-Xuan Cai, [b,c,d] Ting-Ting Cheng, [b,c,d] Li-Peng Zhou, *[b,c,d] and Qing-Fu Sun*[a,b,d]

[a] College of Chemistry, Fuzhou University, Fuzhou 350108, People's Republic of China.

[b] State Key Laboratory of Structural Chemistry, Fujian Institute of Research on the Structure of Matter, Chinese Academy of Sciences, Fuzhou 350002, People's Republic of China.

[c] College of Chemistry and Material Science, Fujian Normal University, Fuzhou 350007, China

[d] Fujian College, University of Chinese Academy of Sciences, Fuzhou 350002, People's Republic of China.

Contents

1. General

Unless otherwise stated, all chemicals and solvents were purchased from commercial companies and used without further purification. Deuterated solvents were purchased from Admas, J&K scientific and Sigma-Aldrich. $H_6\mathbf{L^3}$ was prepared following our previous procedure.[S1] 1D and 2D NMR spectra were measured on a Bruker Biospin Avance III (400 MHz) and Rigaku ECZ600S (600 MHz) spectrometer. ^{1}H-NMR chemical shifts were determined with respect to residual signals of the deuterated solvents used. ESI-TOF-MS spectra were recorded on an Impact II UHR-TOF mass spectrometry from Bruker, with sodium trifluoroacetate as the internal standard. Data analysis was conducted with the Bruker Data Analysis software (Version 4.3) and simulations were performed with the Bruker Isotope Pattern software.

2. Synthetic Procedures

2.1 Experimental details and characterization

Scheme S1 The structures of ligands $H_4\mathbf{L^1}$, $H_4\mathbf{L^2}$, $H_6\mathbf{L^3}$, $H_5\mathbf{L^{3'}}$ and $H_4\mathbf{L^{3''}}$.

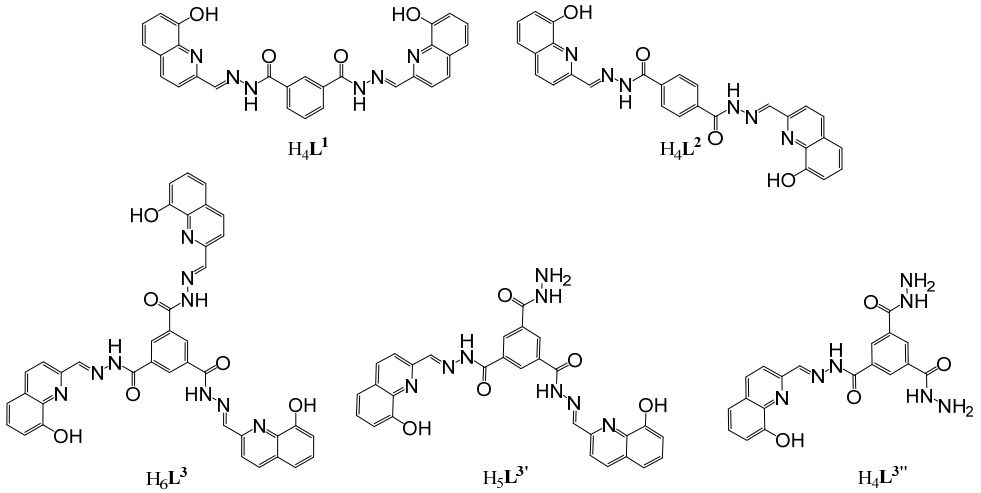

Synthesis of $Ce_3(H_3\mathbf{L^3})_2(OTf)_3$: To a yellow suspension of $H_6\mathbf{L^3}$ (2.32 mg, 3.23 μmol,1.0 equiv) in 500 μL CD_3CN/CD_3OD (v/v=1:1) , $Ce(OTf)_3$ (2.85 mg, 4.85 μmol, 1.5 equiv) was added and then stirred at 50 °C for 1 h. The homogeneous jujube red solution was characterized without further treatment. ESI-TOF-MS: calcd. for $[Ce_3(H_3\mathbf{L^3})_2]^{3+}$ 616.0249, found 616.0289; $[Ce_3(H_3\mathbf{L^3})_2(HOTf)_2]^{3+}$ 715.9978, found 716.0023; calcd. for $[Ce_3(H_3\mathbf{L^3})_2(OTf)_1]^{2+}$ 998.5133, found 998.5182; calcd. for $[Ce_3(H_3\mathbf{L^3})_2(OTf)_1(HOTf)_2]^{2+}$ 1149.4803, found 1149.4802.

Synthesis of $La_3(H_3\mathbf{L^3})_2(OTf)_3$/$La_4(H_3\mathbf{L^3})_2(OTf)_6$: To a yellow suspension of $H_6\mathbf{L^3}$ (2.31 mg, 3.21 μmol,1.0 equiv) in 500 μL CD_3CN/CD_3OD (v/v=1:1) , $La(OTf)_3$ (2.85 mg, 4.86 μmol, 1.5 equiv) was added and then stirred at 50 °C for 1 h. The homogeneous jujube red solution was characterized without further treatment. ESI-TOF-MS: calcd.

for $[La_3(H_3\mathbf{L^3})_2]^{3+}$ 615.0291, found 615.0291; calcd. for $[La_3(H_3\mathbf{L^3})_2(HOTf)_2]^{3+}$ 715.0023, found 715.0024; calcd. for $[La_3(H_3\mathbf{L^3})_2(OTf)_1]^{2+}$ 997.0200, found 997.0203; calcd. for $[La_3(H_3\mathbf{L^3})_2(OTf)_1(HOTf)_2]^{2+}$ 1146.9798, found 1146.9787; calcd. for $[La_4(H_3\mathbf{L^3})_2(OTf)_3]^{3+}$ 810.2833, found 810.2832; calcd. for $[La_6(H_3\mathbf{L^3})_4(OTf)_4]^{2+}$ 1289.9012, found 1289.9019.

Synthesis of $Eu_6(H_3\mathbf{L^3})_4(OTf)_6$: To a yellow suspension of $H_6\mathbf{L^3}$ (2.51 mg, 3.50 μmol,1.0 equiv) in 500 μL CD_3CN/CD_3OD (v/v=1:1) , $Eu(OTf)_3$ (3.15 mg, 5.25 μmol, 1.5 equiv) was added and then stirred at 50 °C for 1 h. The turbid yellow suspension turned clear, and a homogeneous jujube red solution was obtained. This solution was characterized without further treatment. ESI-TOF-MS: calcd. for $[Eu_6(H_3\mathbf{L^3})_4(OTf)_2(HOTf)_{10}]^{4+}$ 1392.1919, found 1392.1893; calcd. for $[Eu_6(H_3\mathbf{L^3})_4(OTf)_2(HOTf)_{11}]^{4+}$ 1429.9319, found 1429.9286; calcd. for $[Eu_6(H_3\mathbf{L^3})_4(OTf)_2(HOTf)_{12}]^{4+}$ 1467.4219, found 1467.4237; calcd. for $[Eu_6(H_3\mathbf{L^3})_4(OTf)_3(HOTf)_4]^{3+}$ 1605.9873, found 1605.9859; calcd. for $[Eu_6(H_3\mathbf{L^3})_4(OTf)_3(HOTf)_5]^{3+}$ 1655.9739, found 1655.9712; calcd. for $[Eu_6(H_3\mathbf{L^3})_4(OTf)_3(HOTf)_6]^{3+}$ 1705.9604, found 1705.9591.

Synthesis of $Eu_6(H_3\mathbf{L^{3'}})_6(OTf)_6$: Single crystals of $Eu_6(H_3\mathbf{L^{3'}})_6(OTf)_6$ were obtained by the slow vapor diffusion of diethyl ether vapor into the CH_3CN/CH_3OH (v/v=1:1) solution of $Eu_6(H_3\mathbf{L^3})_4(OTf)_6$ after one weeks. ESI-TOF-MS: calcd. for $[Eu_6(H_3\mathbf{L^{3'}})_6(OTf)_1]^{5+}$ 884.6824, found 884.6815; calcd. for $[Eu_6(H_3\mathbf{L^{3'}})_6(OTf)_2]^{4+}$ 1143.0911, found 1143.0904; calcd. for $[Eu_6(H_3\mathbf{L^{3'}})_6(OTf)_3]^{3+}$ 1574.1059, found 1574.1048.

Synthesis of $Eu_4(H_3\mathbf{L^3})_2(OTf)_6$: To a yellow suspension of $H_6\mathbf{L^3}$ (2.58 mg, 3.59 μmol,1.0 equiv) in 500 μL CD_3CN/CD_3OD (v:v=1:1) , $Eu(OTf)_3$ (4.31 mg, 7.18 μmol, 2.0 equiv) was added and then stirred at 50 °C for 1 h. The turbid yellow suspension turned clear, and a homogeneous jujube red solution was obtained. Single crystals of $Eu_4(H_3\mathbf{L^3})_2(OTf)_6$ were obtained by the slow vapor diffusion of diethyl ether vapor into the CH_3CN/CH_3OH (v/v=1:1) solution after one weeks.

Synthesis of $(Et_4N)_6Ce_6\mathbf{L^3}_4$: To a yellow solution of $H_6\mathbf{L^3}$ (14.80 mg, 20.62 μmol) in 500 μL *d*6-DMSO, $Ce(OTf)_3$ (18.19 mg, 30.97 μmol, 1.5 equiv) and tetraethylammonium hydroxide (25 wt.% aqueous solution, 73 μL, 123.93 μmol, 6 equiv) was added and then stirred at 50 °C for 1 h. This homogeneous jujube red solution was characterized without further treatment. ESI-TOF-MS: calcd. for $[(Et_4N)_1Ce_6\mathbf{L^3}_4]^{5-}$ 763.4497, found 763.4507; calcd. for $[(Et_4N)_2Ce_6\mathbf{L^3}_4]^{4-}$ 986.8519, found 986.8524; calcd. for $[(Et_4N)_3Ce_6\mathbf{L^3}_4]^{3-}$ 1359.1889, found 1359.1890.

The complex $(Et_4N)_6La_6\mathbf{L^3}_4$ was prepared by a similar procedure only changing the metal source with $La(OTf)_3$.

$(Et_4N)_6La_6\mathbf{L^3}_4$: ESI-TOF-MS: calcd. for $[(Et_4N)_1La_6\mathbf{L^3}_4]^{5-}$ 761.8499, found 761.8496; calcd. for $[(Et_4N)_1H_1La_6\mathbf{L^3}_4]^{4-}$ 952.5641, found 952.5632; calcd. for $[(Et_4N)_2La_6\mathbf{L^3}_4]^{4-}$ 985.1028, found 985.1018; calcd. for $[(Et_4N)_1H_2La_6\mathbf{L^3}_4]^{3-}$ 1270.4213, found 1270.4193; calcd. for $[(Et_4N)_2H_1La_6\mathbf{L^3}_4]^{3-}$ 1313.8062, found 1313.8042; calcd. for $[(Et_4N)_3La_6\mathbf{L^3}_4]^{3-}$ 1356.8568, found 1356.8547.

Synthesis of Δ_6/Λ_6-$(Et_4N)_6Ln_6\mathbf{L^3}_4$: To a small vial was added a DMSO solution of $H_6\mathbf{L^3}$

(200 μL, 63 mg/mL, 17.53 μmol), $Ce(OTf)_3$ (203 μL, 80 mg/mL in DMSO, 26.30 μmol, 1.5 equiv), tetraethylammonium hydroxide (25 wt.% aqueous solution, 62 μL, 105.18 μmol, 6 equiv). The resulting homogeneous jujube red solution of $(Et_4N)_6Ce_6\mathbf{L^3}_4$ was further stirred at 50°C, during which a red insoluble gradually precipitated from the solution. After 24 hours, the precipitation was collected by centrifugation and redissolved in *d*6-DMSO for further ^{1}H NMR characterization.

***Δ*6/*Λ*6-$(Et_4N)_6Ce_6\mathbf{L^3}_4$:** *Δ*6/*Λ*6-$(Et_4N)_6Ce_6\mathbf{L^3}_4$ was synthesized by method A. ^{1}H NMR (400 MHz, *d*6-DMSO, 298 K) δ 14.38 (s, 1H), 9.66 (s, 1H), 8.32 (s, 2H), 7.44 (s, 1H), 7.00 (d, *J* = 7.6 Hz, 1H), 6.49 (d, *J* = 7.3 Hz, 1H), 4.17 (d, *J* = 7.4 Hz, 1H). ESI-TOF-MS: calcd. for $[(Et_4N)_1Ce_6\mathbf{L^3}_4]^{5-}$ 763.4497, found 763.4492; calcd. for $[(Et_4N)_2Ce_6\mathbf{L^3}_4]^{4-}$ 986.8519, found 986.8503; calcd. for $[(Et_4N)_3Ce_6\mathbf{L^3}_4]^{3-}$ 1359.1889, found 1359.1864.

***Δ*6/*Λ*6-$(Et_4N)_6La_6\mathbf{L^3}_4$:** *Δ*6/*Λ*6-$(Et_4N)_6La_6\mathbf{L^3}_4$ was synthesized by method A. ^{1}H NMR (400 MHz, DMSO, 298K) δ 8.79 (s, 1H), 8.52 (d, *J* = 7.9 Hz, 1H), 8.51 (s, 1H), 7.82 (d, *J* = 8.4 Hz, 1H), 7.23 (t, *J* = 7.8 Hz, 1H), 6.91 (d, *J* = 7.9 Hz, 1H), 6.23 (d, *J* = 7.7 Hz, 1H). ESI-TOF-MS: ESI-TOF-MS: calcd. for $[H_2La_6\mathbf{L^3}_4]^{4-}$ 920.2762, found 920.2761; $[H_3La_6\mathbf{L^3}_4]^{3-}$ 1127.3707, found 1127.3701; calcd. for $[(Et_4N)_1H_2La_6\mathbf{L^3}_4]^{3-}$ 1270.4213, found 1270.4203; calcd. for $[(Et_4N)_2H_1La_6\mathbf{L^3}_4]^{3-}$ 1313.8062, found 1313.8048; calcd. for $[(Et_4N)_1H_3La_6\mathbf{L^3}_4]^{2-}$ 1906.1356, found 1906.1348.

The yields at different reaction times are summarized below:

Table S1 The yields of *Δ*6/*Λ*6-$La_6\mathbf{L^3}_4$ and *Δ*6/*Λ*6-$Ce_6\mathbf{L^3}_4$ in different reaction duration.

Duration	Yield(%)	
	*Δ*6/*Λ*6-$La_6\mathbf{L^3}_4$	*Δ*6/*Λ*6-$Ce_6\mathbf{L^3}_4$
6 hours	37.1	16.7
12 hours	56.8	30.4
24 hours	57.1	35.4

2.2 NMR spectra

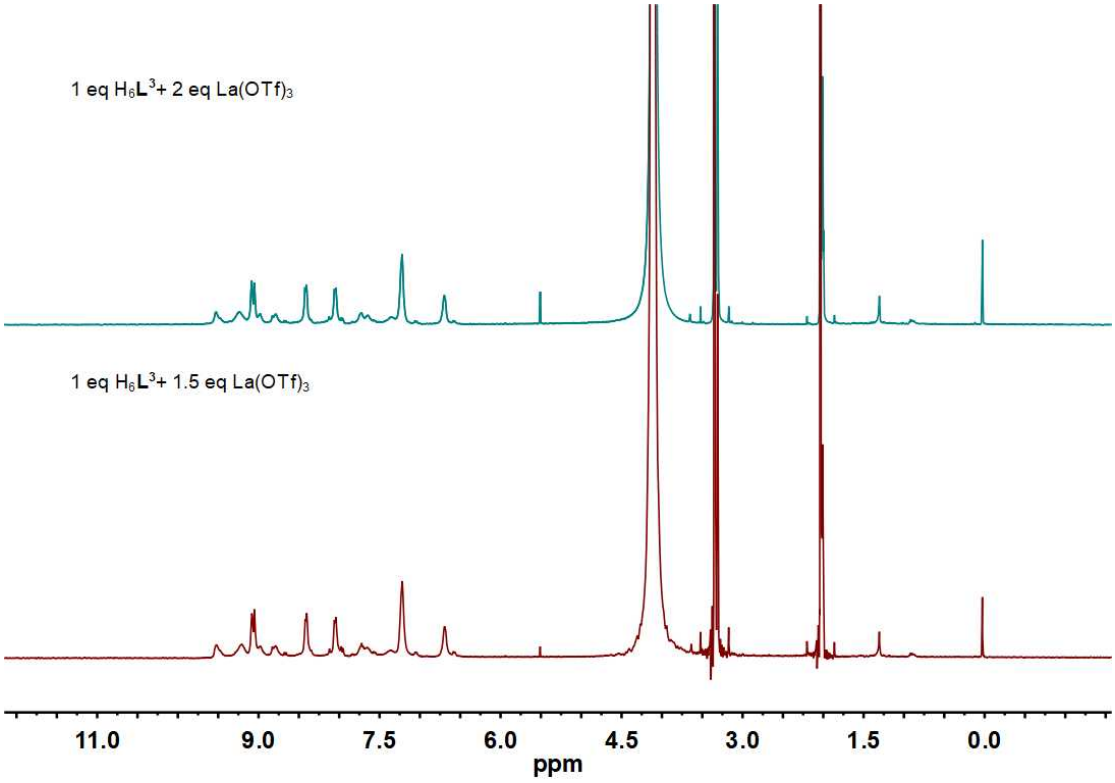

Figure S1 ^{1}H NMR spectrum of $La_3(H_3\mathbf{L}^3)_2(OTf)_3$/$La_4(H_3\mathbf{L}^3)_2(OTf)_6$ (400 MHz, CD_3CN/CD_3OD v/v = 1/1, 298 K).

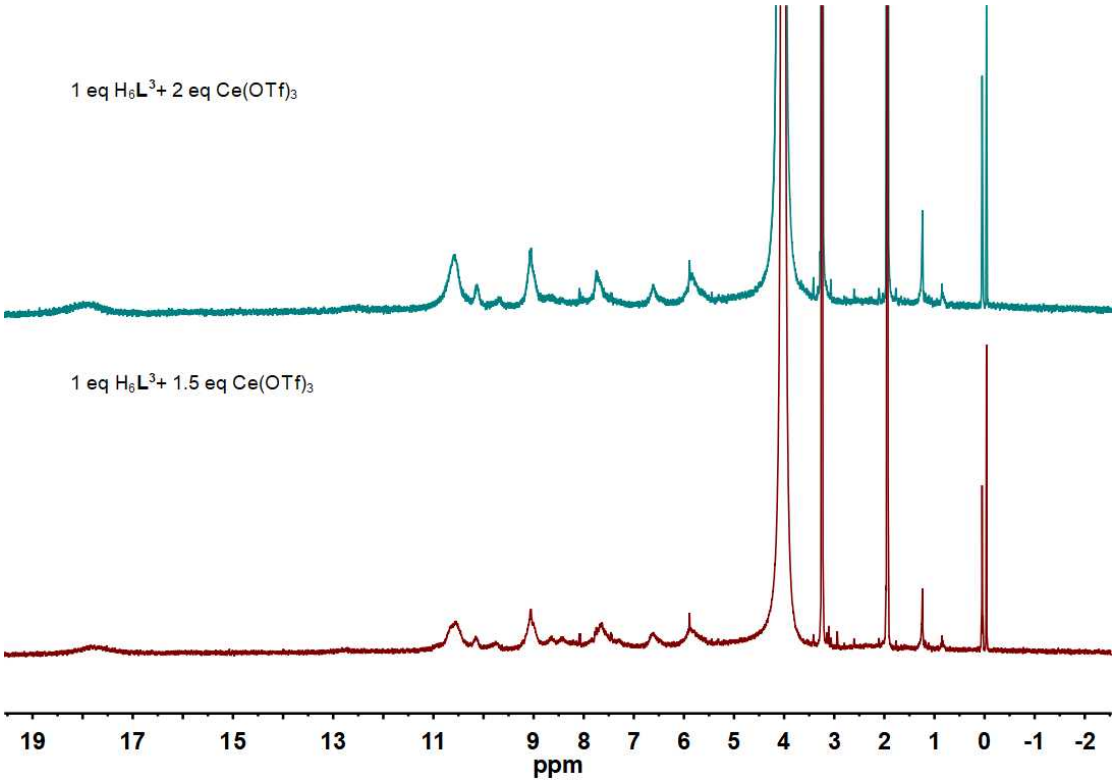

Figure S2 ^{1}H NMR spectrum of $Ce_3(H_3\mathbf{L}^3)_2(OTf)_3$ (400 MHz, CD_3CN/CD_3OD v/v =

1/1, 298 K).

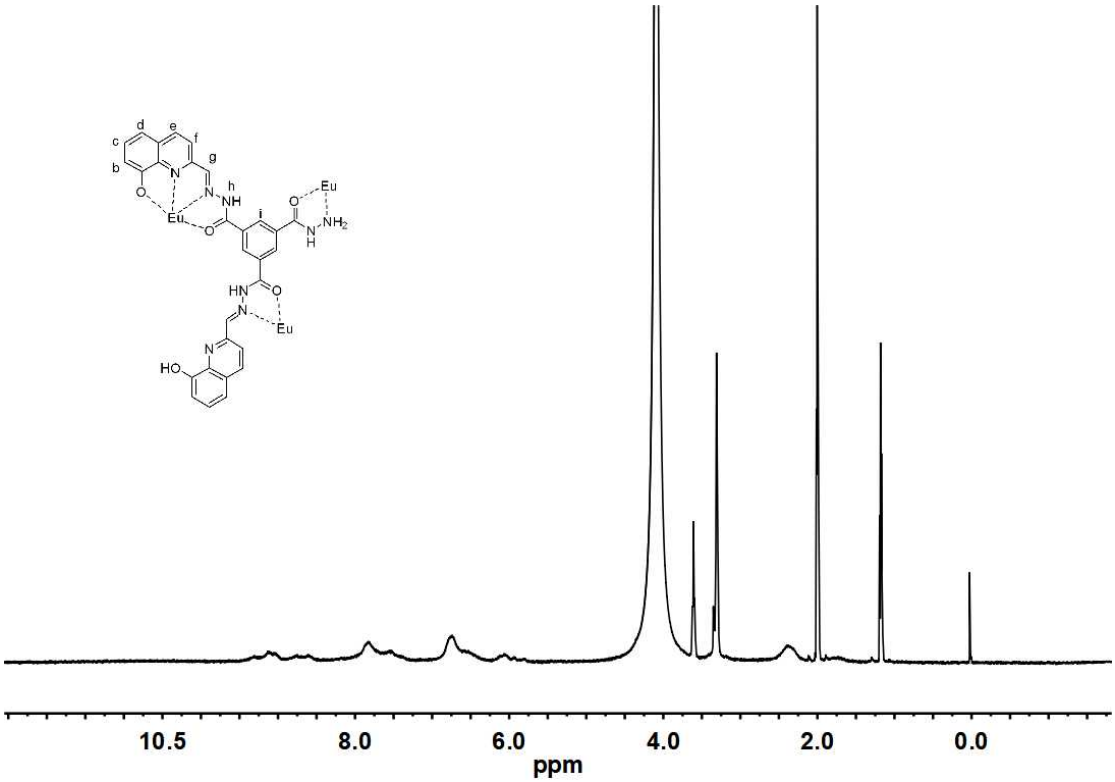

Figure S3 ^{1}H NMR spectrum of $Eu_6(H_3\mathbf{L}^{3'})_6(OTf)_6$ crystal (400 MHz, CD_3CN/CD_3OD v/v = 1/1, 298 K).

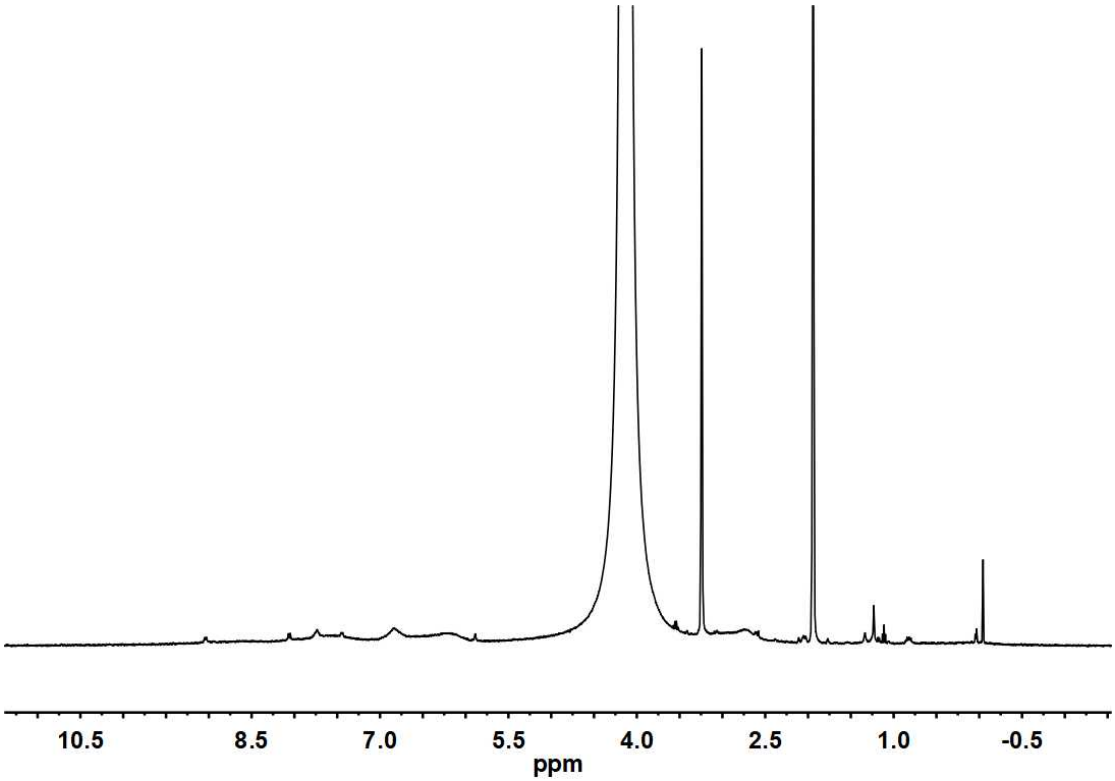

Figure S4 ^{1}H NMR spectrum of $Eu_3(H_3\mathbf{L}^{3})_2(OTf)_3$/$Eu_4(H_3\mathbf{L}^{3})_2(OTf)_6$ (400 MHz, CD_3CN/CD_3OD v/v = 1/1, 298 K).

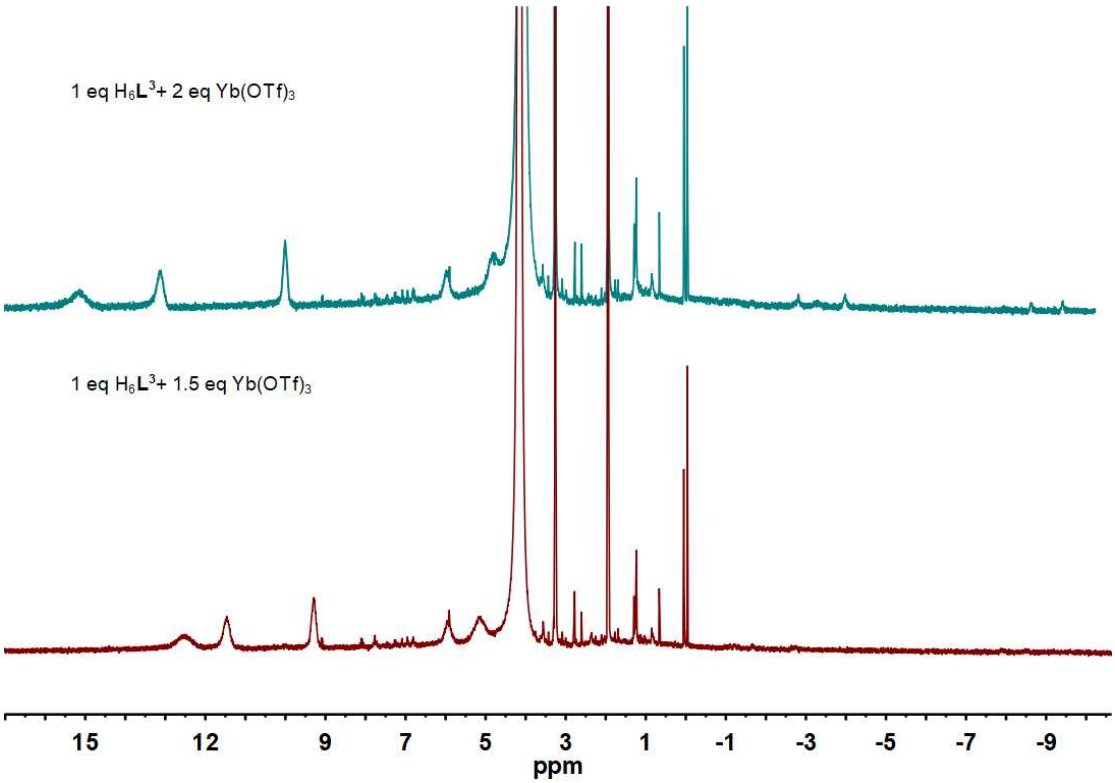

Figure S5 ^{1}H NMR spectrum of $Yb_6(H_3\mathbf{L}^3)_4(OTf)_6$ (400 MHz, CD_3CN/CD_3OD v/v = 1/1, 298 K).

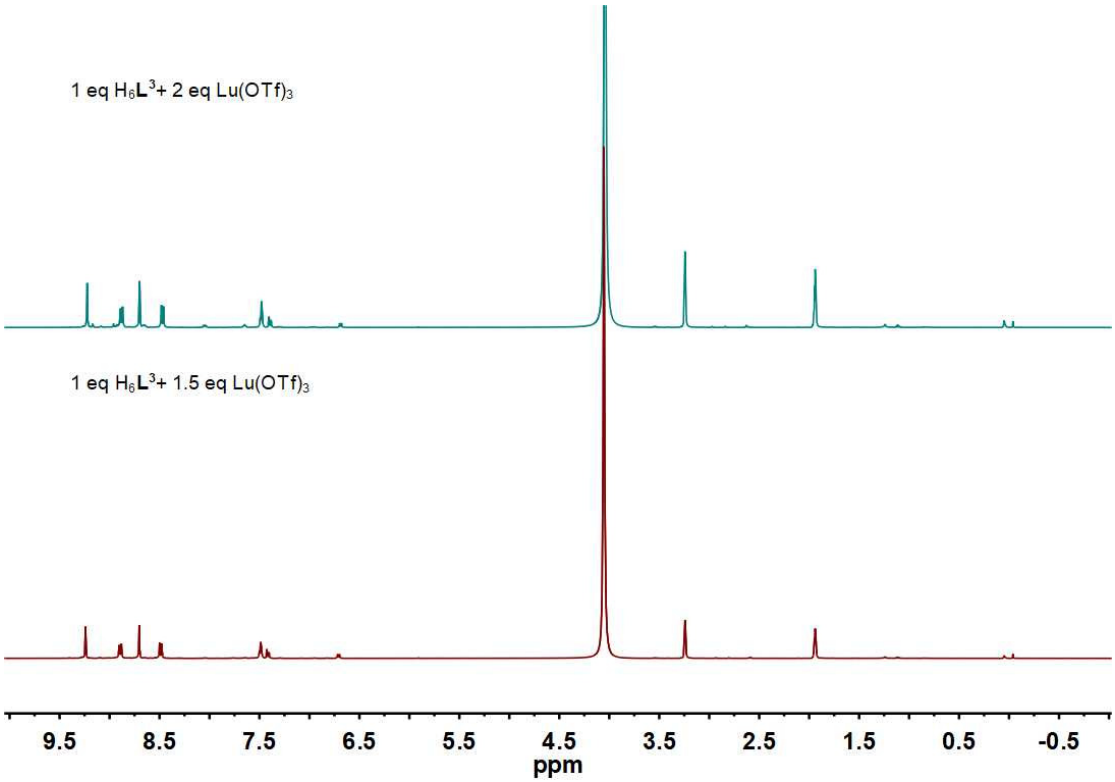

Figure S6 ^{1}H NMR spectrum of $Lu_6(H_3\mathbf{L}^3)_4(OTf)_6$ (400 MHz, CD_3CN/CD_3OD v/v = 1/1, 298 K).

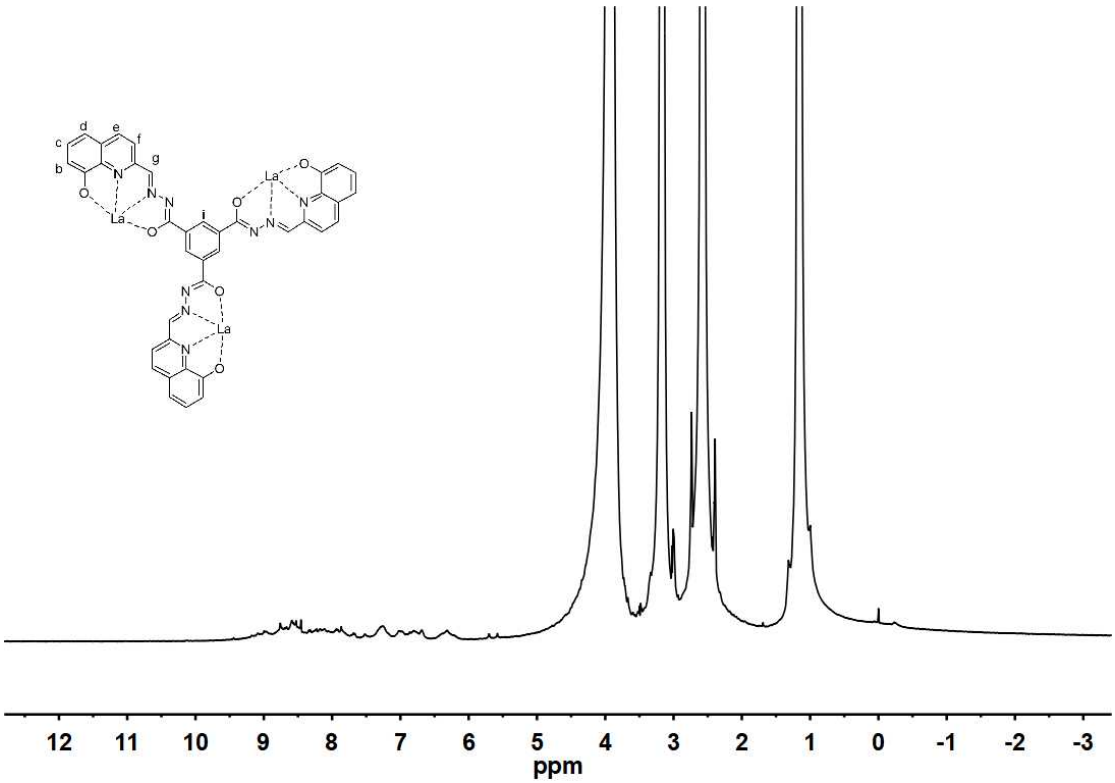

Figure S7 ^{1}H NMR spectrum of $(Et_4N)_6La_6\mathbf{L}^{3}_4$ (400 MHz, *d*$_6$-DMSO, 298 K).

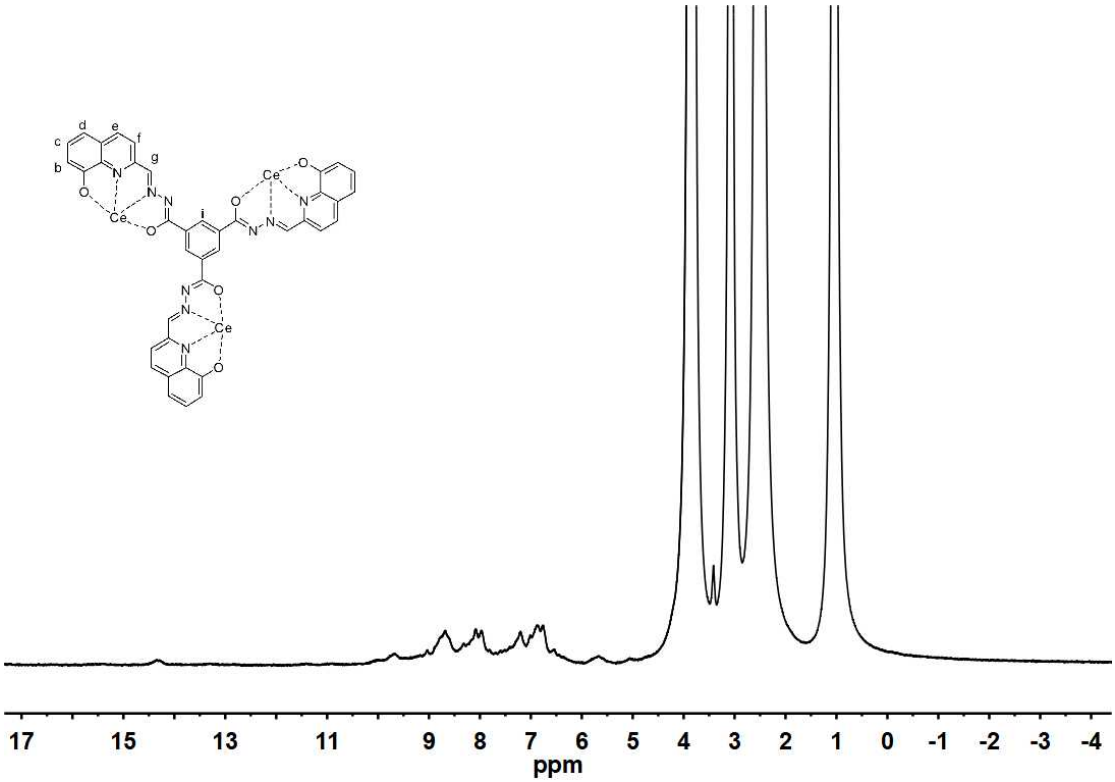

Figure S8 ^{1}H NMR spectrum of $(Et_4N)_6Ce_6\mathbf{L}^{3}_4$ (400 MHz, *d*$_6$-DMSO, 298 K).

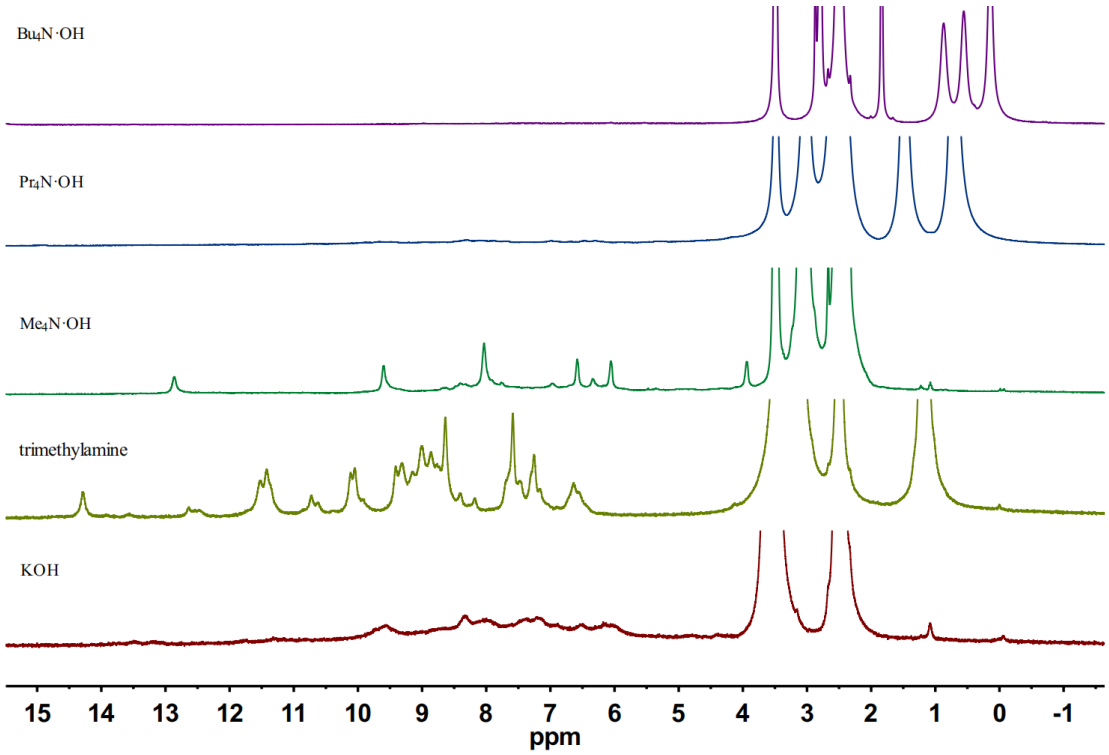

Figure S9 ^{1}H NMR spectrum of the assemblies in the presence of different base (400 MHz, *d*$_6$-DMSO, 298 K).

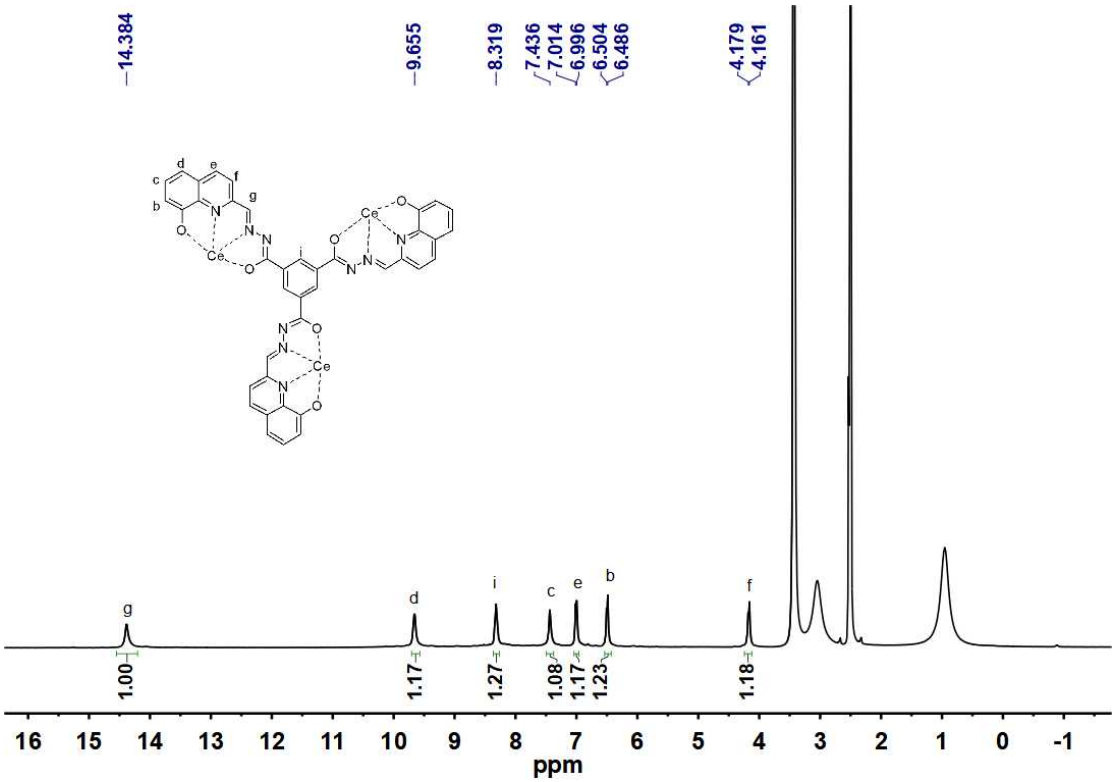

Figure S10 ^{1}H NMR spectrum of *Λ*$_6$/*Λ*$_6$-(Et$_4$N)$_6$Ce$_6$**L**$^{3}_{4}$ (400 MHz, *d*$_6$-DMSO, 298 K).

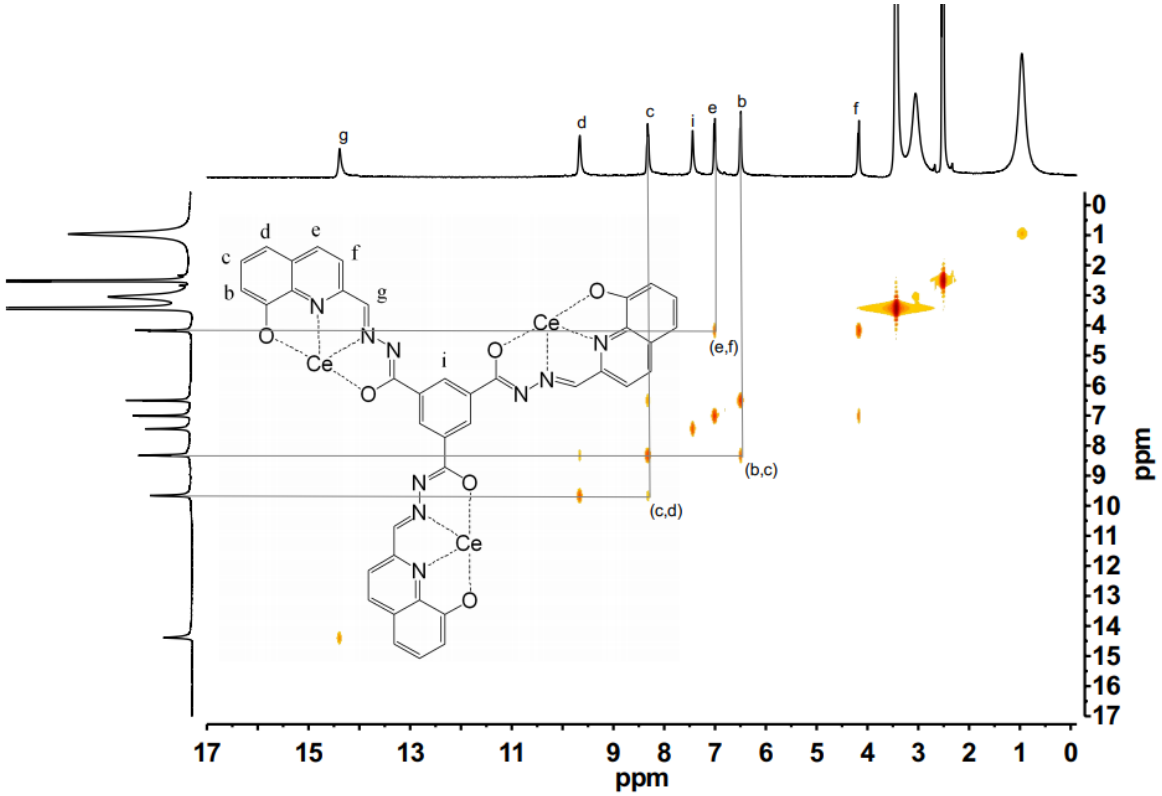

Figure S11 ^{1}H-^{1}H COSY spectrum of Δ_6/Λ_6-$(Et_4N)_6Ce_6\mathbf{L}^{3}_4$ (400 MHz, d_6-DMSO, 298 K).

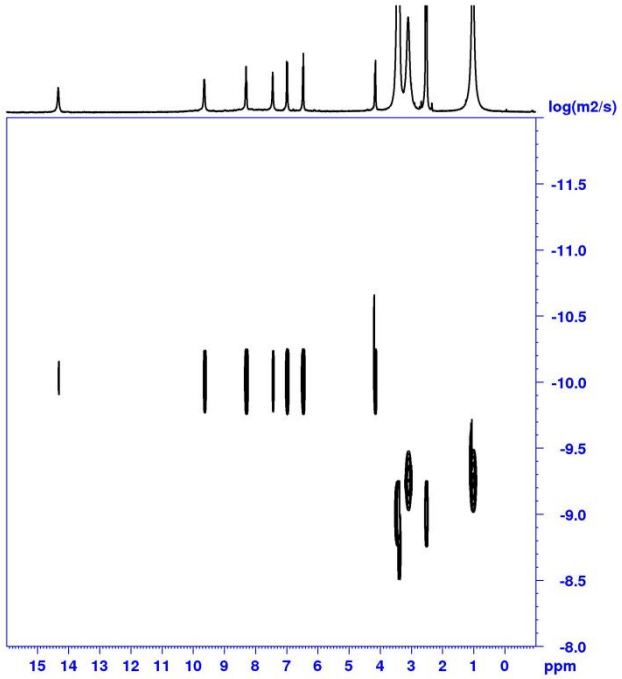

Fig. S12 ^{1}H DOSY spectrum of Δ_6/Λ_6-$(Et_4N)_6Ce_6\mathbf{L}^{3}_4$ ($D=9.71\times10^{-11}$ m^2s^{-1}, r = 11.31 Å, 400 MHz, d_6-DMSO, 298 K).

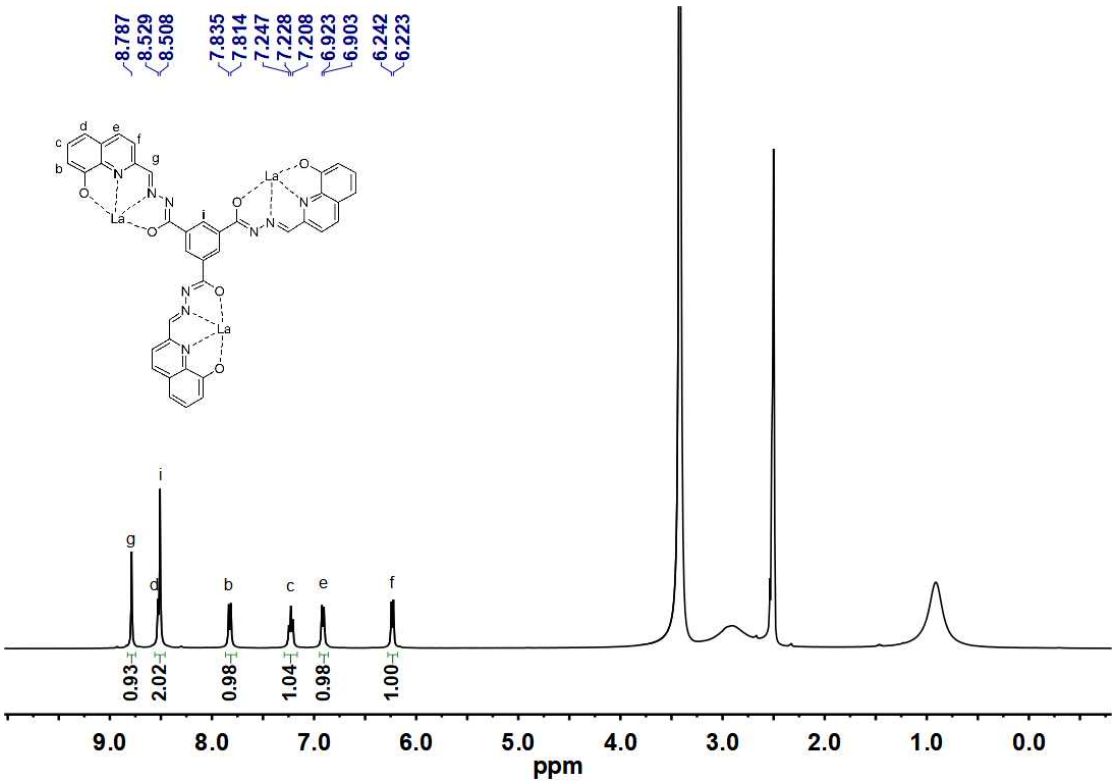

Figure S13 ^{1}H NMR spectrum of Δ_6/Λ_6-$(Et_4N)_6La_6\mathbf{L}^{3}_4$ (400 MHz, d_6-DMSO, 298 K).

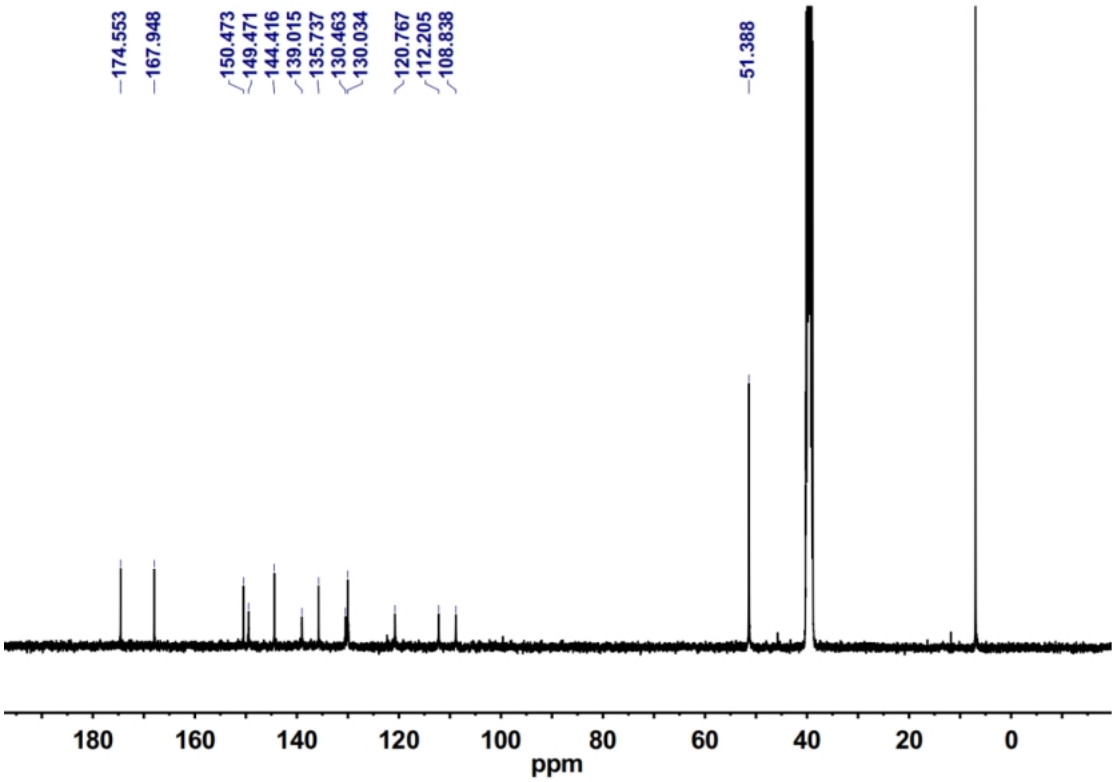

Figure S14 ^{13}C NMR spectrum of Δ_6/Λ_6-$(Et_4N)_6La_6\mathbf{L^3}_4$ (101 MHz, d_6-DMSO, 298K).

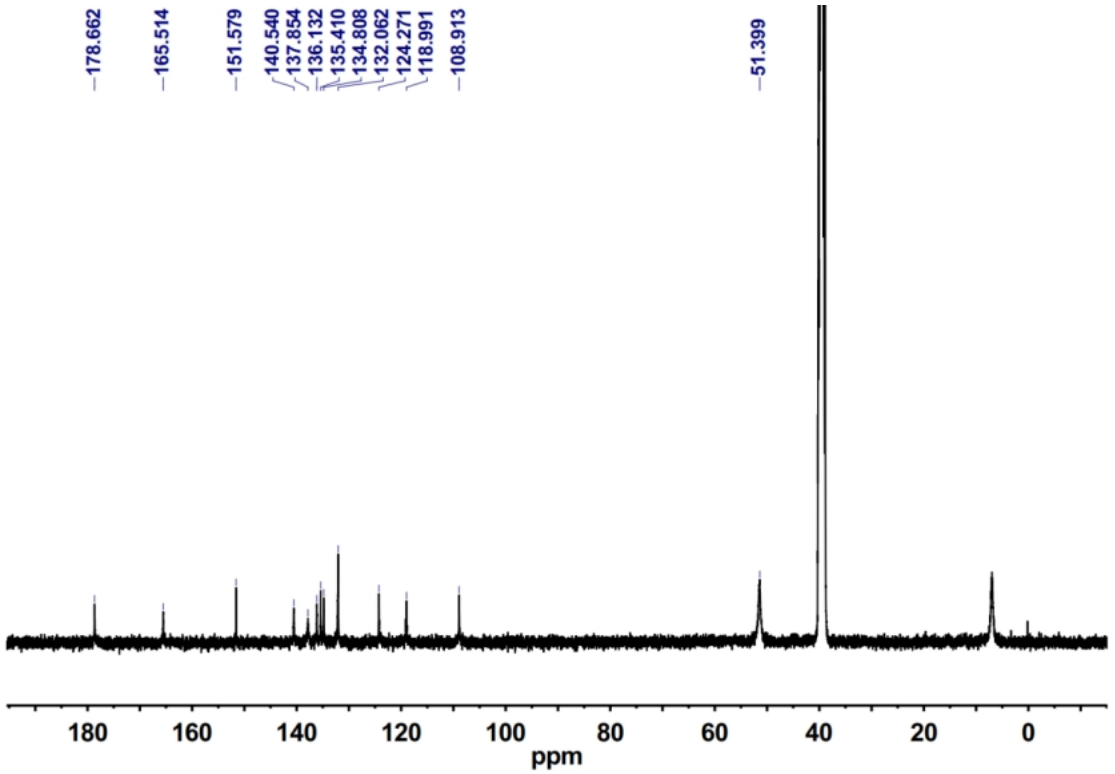

Figure S15 ^{13}C NMR spectrum of Δ_6/Λ_6-$(Et_4N)_6Ce_6\mathbf{L^3}_4$ (101 MHz, d_6-DMSO, 298K).

2.3 ESI-TOF-MS spectra

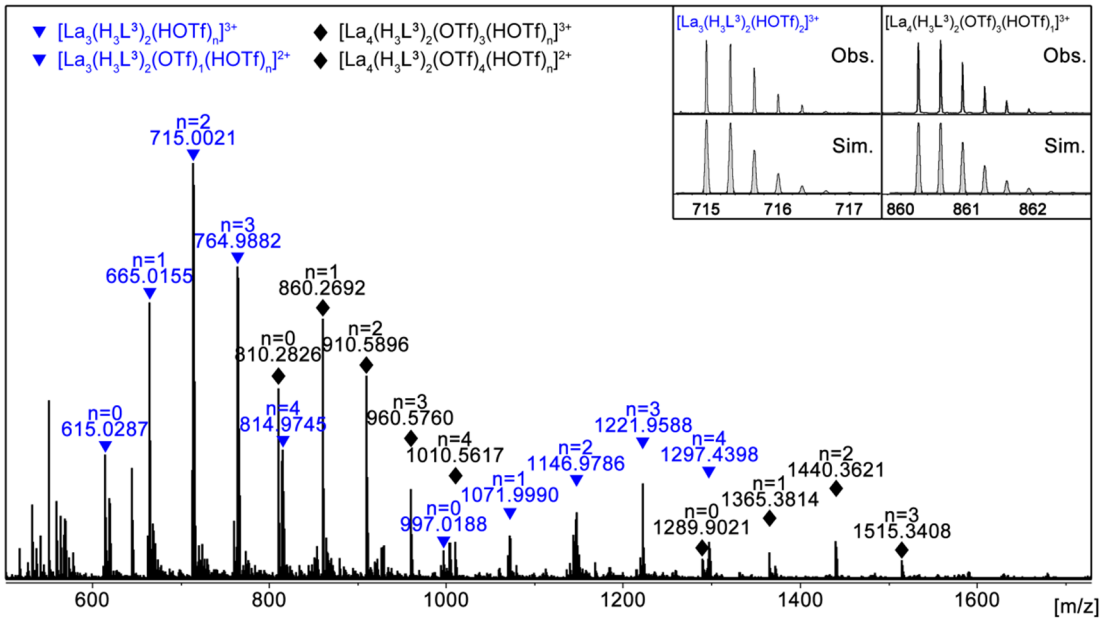

Figure S16 ESI-TOF-MS of $La_3(H_3\mathbf{L^3})_2(OTf)_3/La_4(H_3\mathbf{L^3})_2(OTf)_6$ (assembly in metal/ligand stoichiometric ratio=3:2) with the observed and simulated isotopic patterns of the peaks corresponding to $[La_3(H_3\mathbf{L^3})_2(HOTf)_2]^{3+}$ and $[La_4(H_3\mathbf{L^3})_2(OTf)_3]^{3+}$, respectively.

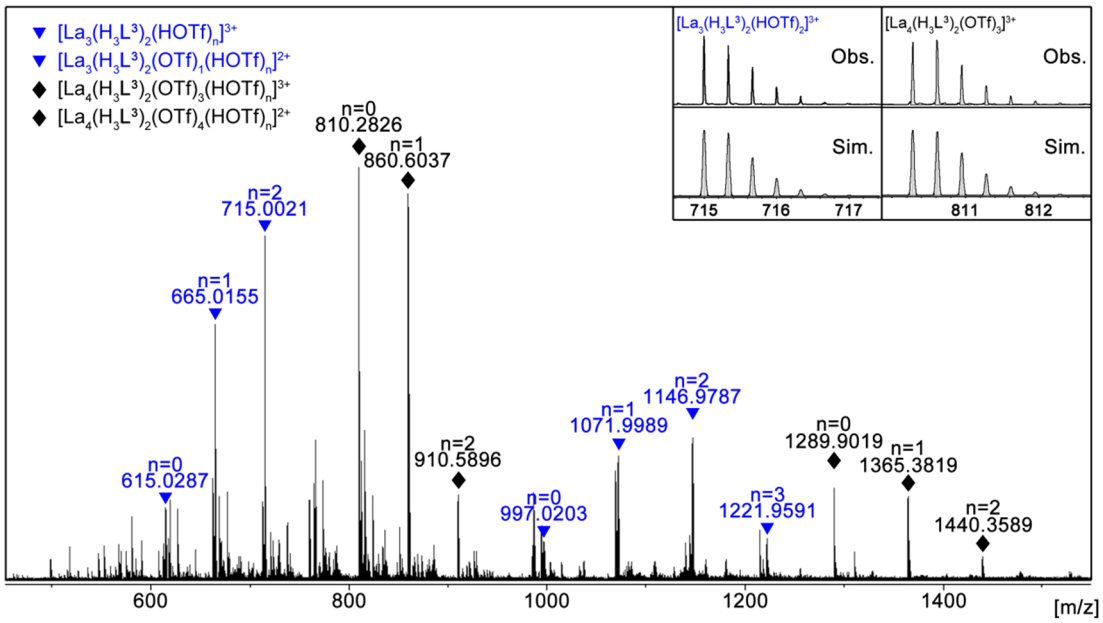

Figure S17 ESI-TOF-MS of $La_3(H_3\mathbf{L^3})_2(OTf)_3/La_4(H_3\mathbf{L^3})_2(OTf)_6$ (assembly in metal/ligand stoichiometric ratio=4:2) with the observed and simulated isotopic patterns of the peaks corresponding to $[La_3(H_3\mathbf{L^3})_2(HOTf)_2]^{3+}$ and $[La_4(H_3\mathbf{L^3})_2(OTf)_3]^{3+}$, respectively.

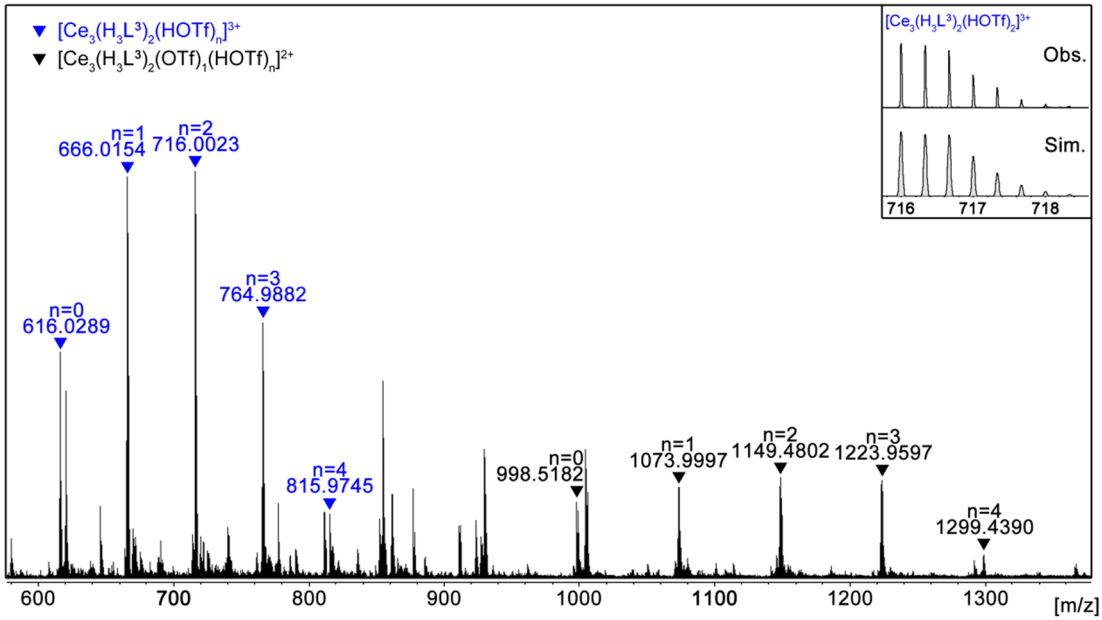

Figure S18 ESI-TOF-MS of $Ce_3(H_3\mathbf{L^3})_2(OTf)_3$ (assembly in metal/ligand stoichiometric ratio=3:2) with the observed and simulated isotopic patterns of the peak corresponding to $[Ce_3(H_3\mathbf{L^3})_2(HOTf)_2]^{3+}$.

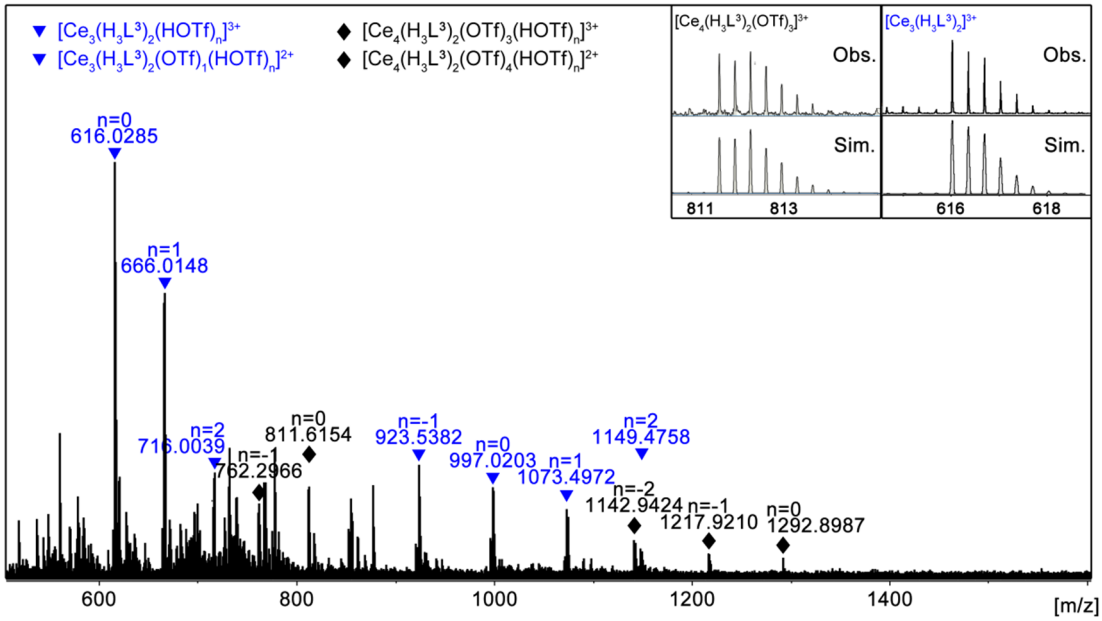

Figure S19 ESI-TOF-MS of $Ce_3(H_3\mathbf{L^3})_2(OTf)_3/Ce_4(H_3\mathbf{L^3})_2(OTf)_6$ (assembly in metal/ligand stoichiometric ratio=4:2) with the observed and simulated isotopic patterns of the peaks corresponding to $[Ce_3(H_3\mathbf{L^3})_2]^{3+}$and $[Ce_4(H_3\mathbf{L^3})_2(OTf)_3]^{3+}$, respectively.

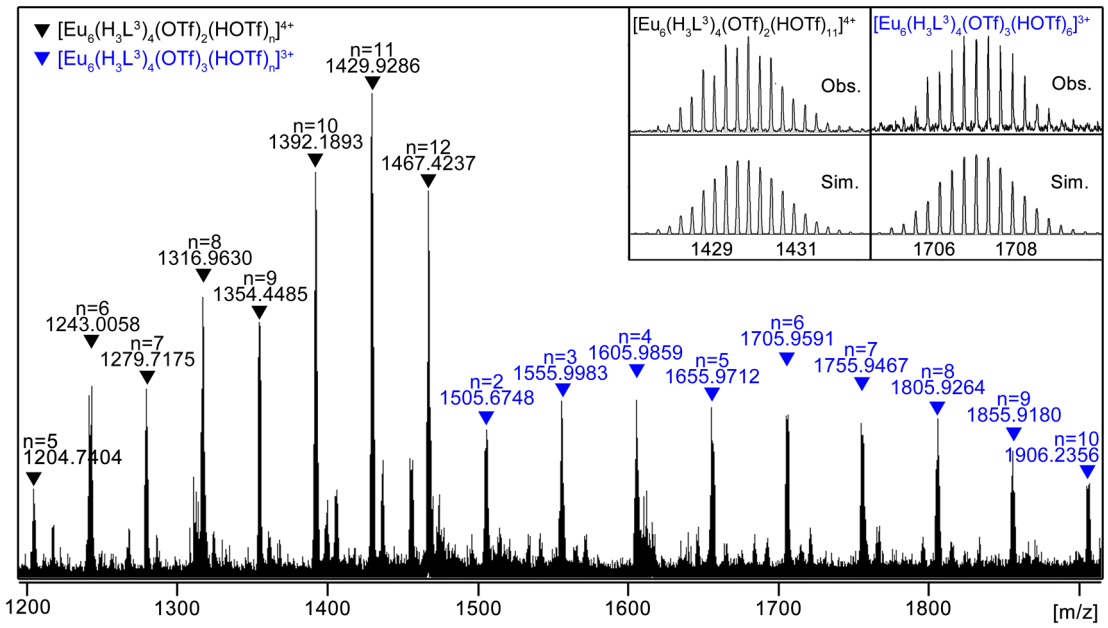

Figure S20 ESI-TOF-MS of $Eu_6(H_3\mathbf{L^3})_4(OTf)_6$ (assembly in metal/ligand stoichiometric ratio=3:2) with the observed and simulated isotopic patterns of the peaks corresponding to $[Eu_6(H_3\mathbf{L^3})_4(OTf)_2(HOTf)_{11}]^{4+}$ and $[Eu_6(H_3\mathbf{L^3})_4(OTf)_3(HOTf)_6]^{3+}$, respectively.

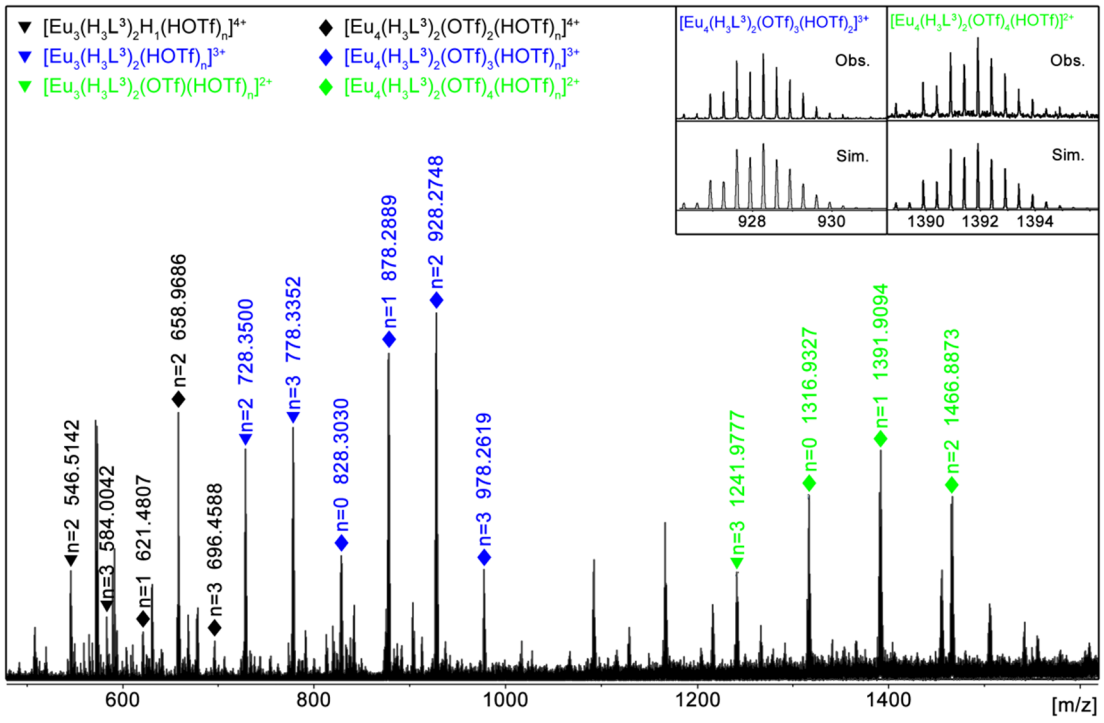

Figure S21 ESI-TOF-MS of $Eu_3(H_3\mathbf{L^3})_2(OTf)_3$/$Eu_4(H_3\mathbf{L^3})_2(OTf)_6$ (assembly in metal/ligand stoichiometric ratio=4:2) with the observed and simulated isotopic patterns of the peaks corresponding to $[Eu_4(H_3\mathbf{L^3})_2(OTf)_4(HOTf)_2]^{3+}$and $[Eu_4(H_3\mathbf{L^3})_2(OTf)_4(HOTf)]^{2+}$, respectively.

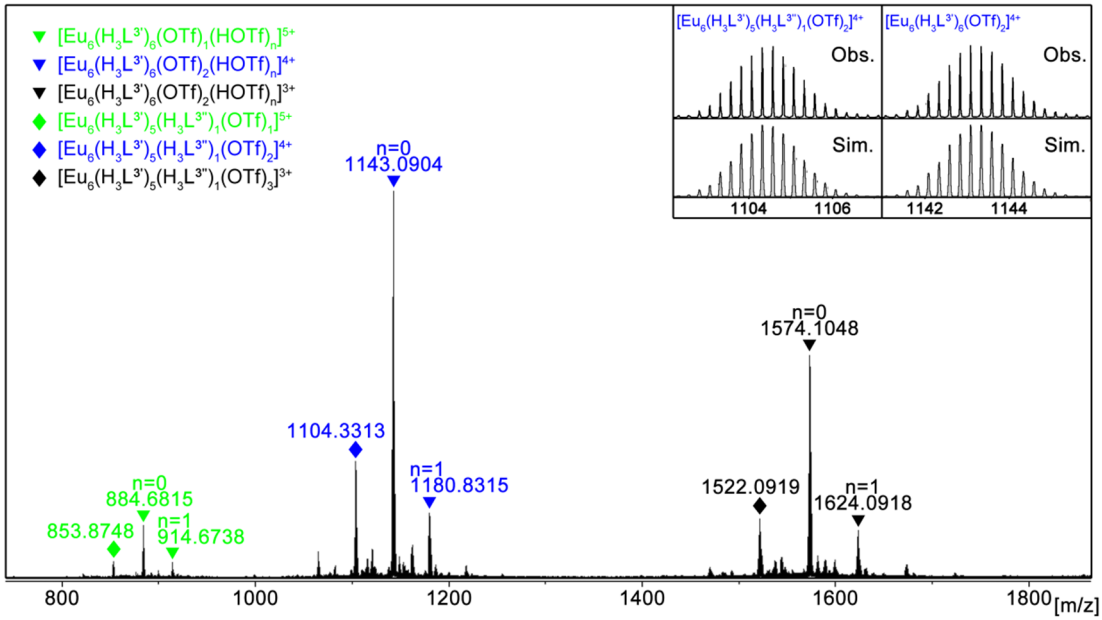

Figure S22 ESI-TOF-MS of $Eu_6(H_3\mathbf{L^{3'}})_6(OTf)_6$ with the observed and simulated isotopic patterns of the peaks corresponding to $[Eu_6(H_3\mathbf{L^{3'}})_5(H_3\mathbf{L^{3''}})_1(OTf)_2]^{4+}$ and $[Eu_6(H_3\mathbf{L^{3'}})_6(OTf)_2]^{4+}$, respectively.

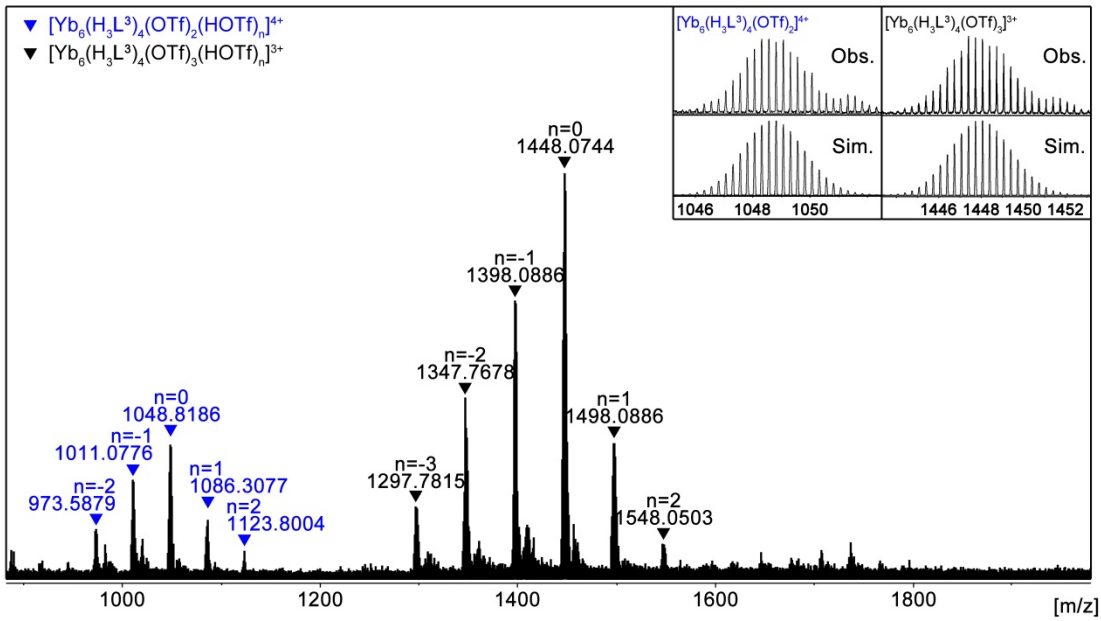

Figure S23 ESI-TOF-MS of $Yb_6(H_3L^3)_4(OTf)_6$ (assembly in metal/ligand stoichiometric ratio=4:2) with the observed and simulated isotopic patterns of the peaks corresponding to $[Yb_6(H_3\mathbf{L^3})_4(OTf)_2]^{4+}$ and $[Yb_6(H_3\mathbf{L^3})_4(OTf)_3]^{3+}$, respectively.

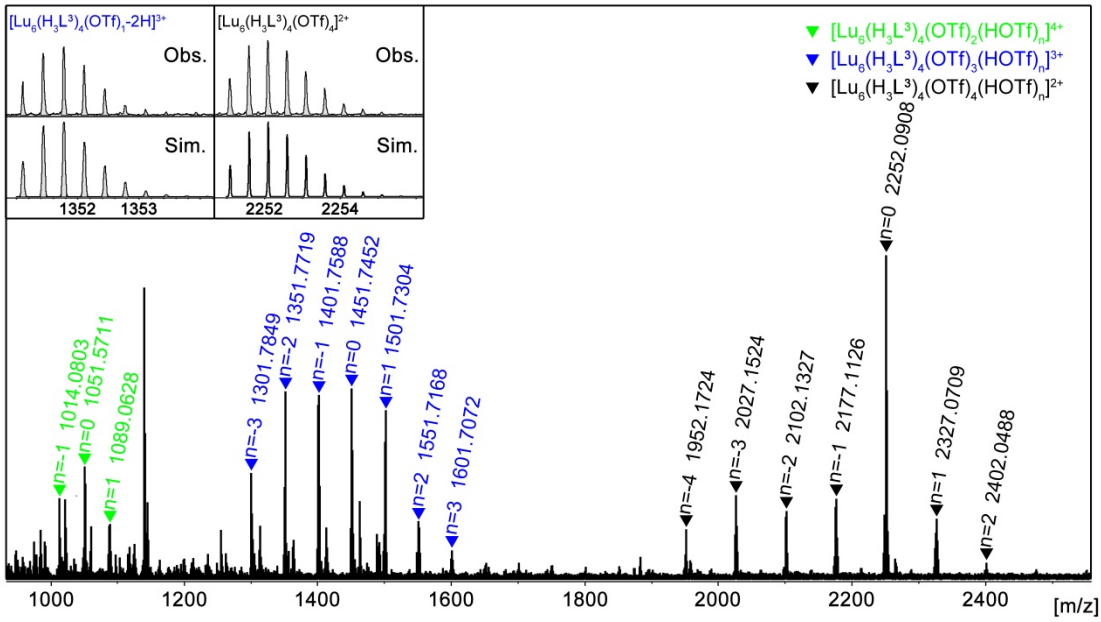

Figure S24 ESI-TOF-MS of $Lu_6(H_3L^3)_4(OTf)_6$ (assembly in metal/ligand stoichiometric ratio=4:2) with the observed and simulated isotopic patterns of the peaks corresponding to $[Lu_6(H_3\mathbf{L^3})_4(OTf)_1\text{-}2H]^{3+}$ and $[Lu_6(H_3\mathbf{L^3})_4(OTf)_4]^{2+}$, respectively.

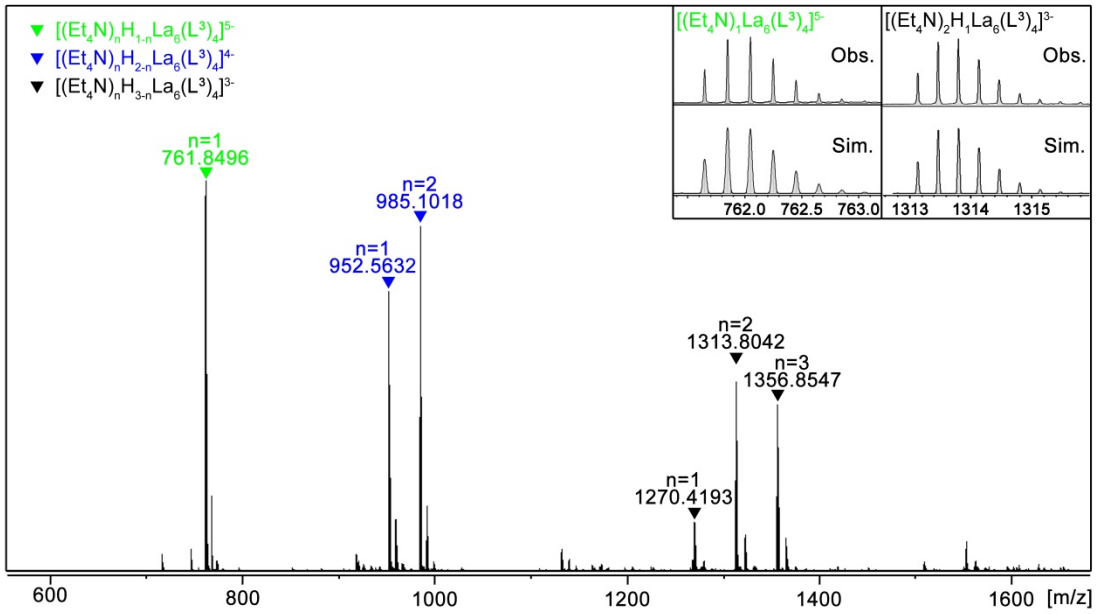

Figure S25 ESI-TOF-MS of $(Et_4N)_6La_6\mathbf{L^3}_4$ with the observed and simulated isotopic patterns of the peaks corresponding to $[(Et_4N)_1La_6\mathbf{L^3}_4]^{5-}$ and $[(Et_4N)_2H_1La_6\mathbf{L^3}_4]^{3-}$, respectively.

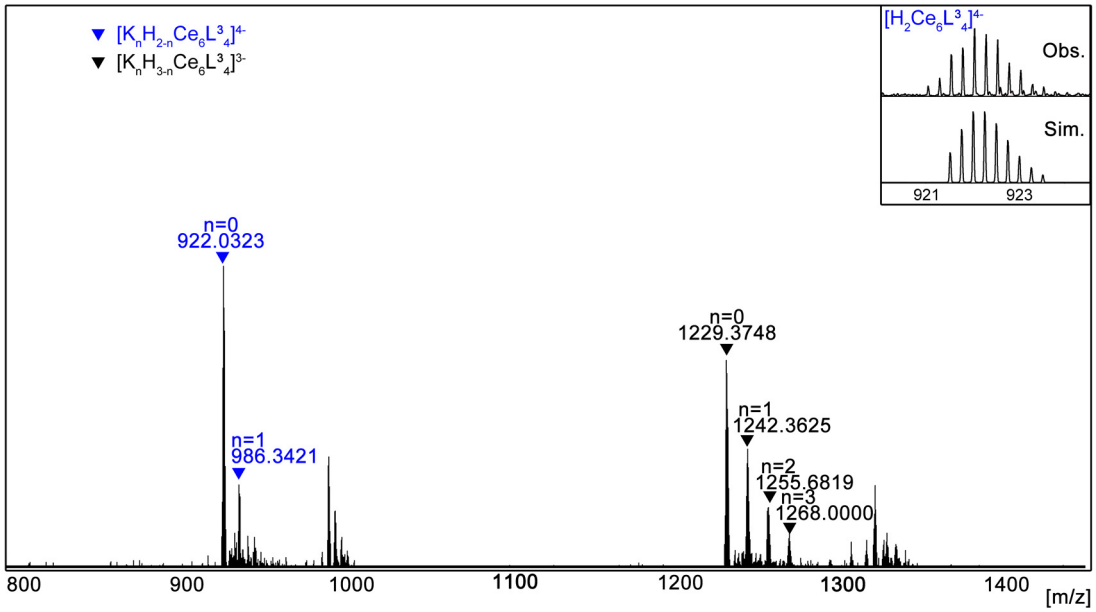

Figure S26 ESI-TOF-MS of $K_6Ce_6\mathbf{L^3}_4$ with the observed and simulated isotopic patterns of the peaks corresponding to $[H_2Ce_6\mathbf{L^3}_4]^{4-}$.

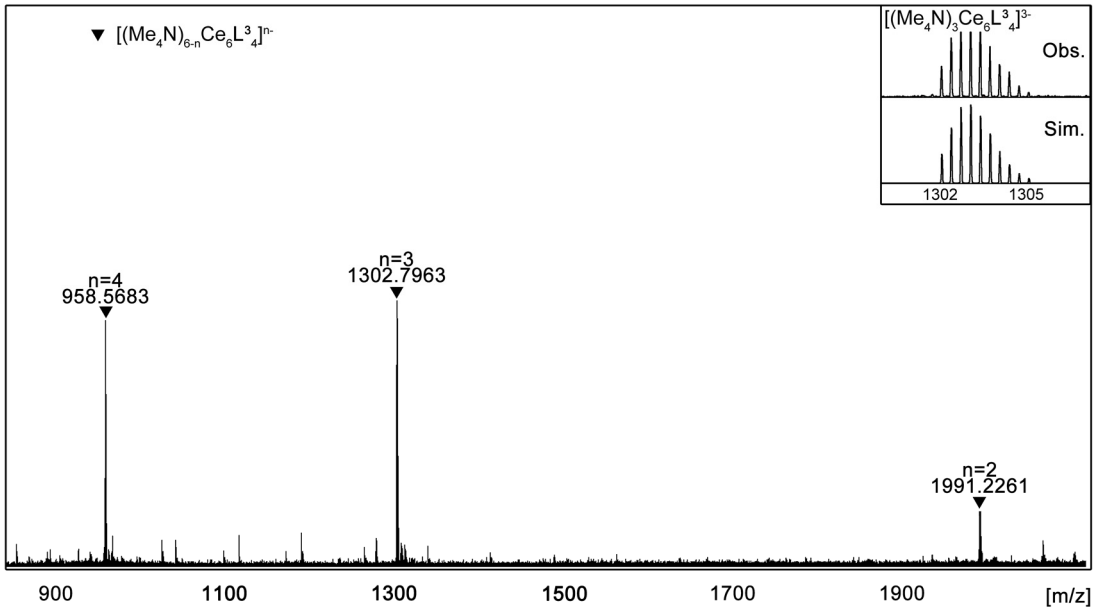

Figure S27 ESI-TOF-MS of $(Me_4N)_6Ce_6\mathbf{L^3}_4$ with the observed and simulated isotopic patterns of the peaks corresponding to $[(Me_4N)_3Ce_6\mathbf{L^3}_4]^{3-}$.

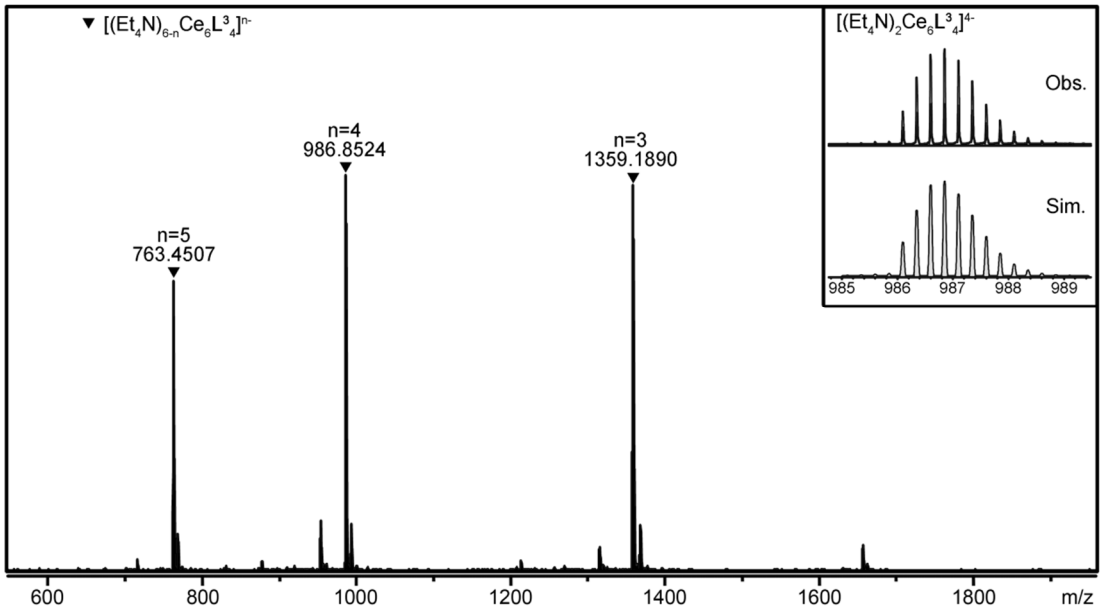

Figure S28 ESI-TOF-MS of $(Et_4N)_6Ce_6\mathbf{L}^{\mathbf{3}}{}_4$ with the observed and simulated isotopic patterns of the peak corresponding to $[(Et_4N)_2Ce_6\mathbf{L}^{\mathbf{3}}{}_4]^{4-}$.

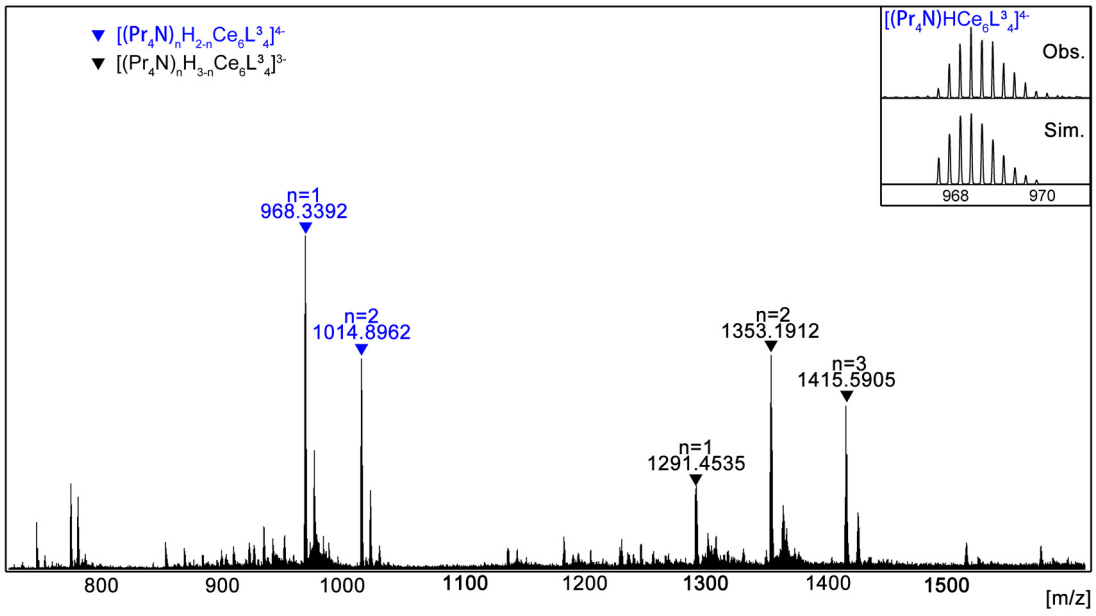

Figure S29 ESI-TOF-MS of $(Pr_4N)_6Ce_6\mathbf{L}^{\mathbf{3}}{}_4$ with the observed and simulated isotopic patterns of the peaks corresponding to $[(Pr_4N)HCe_6\mathbf{L}^{\mathbf{3}}{}_4]^{4-}$.

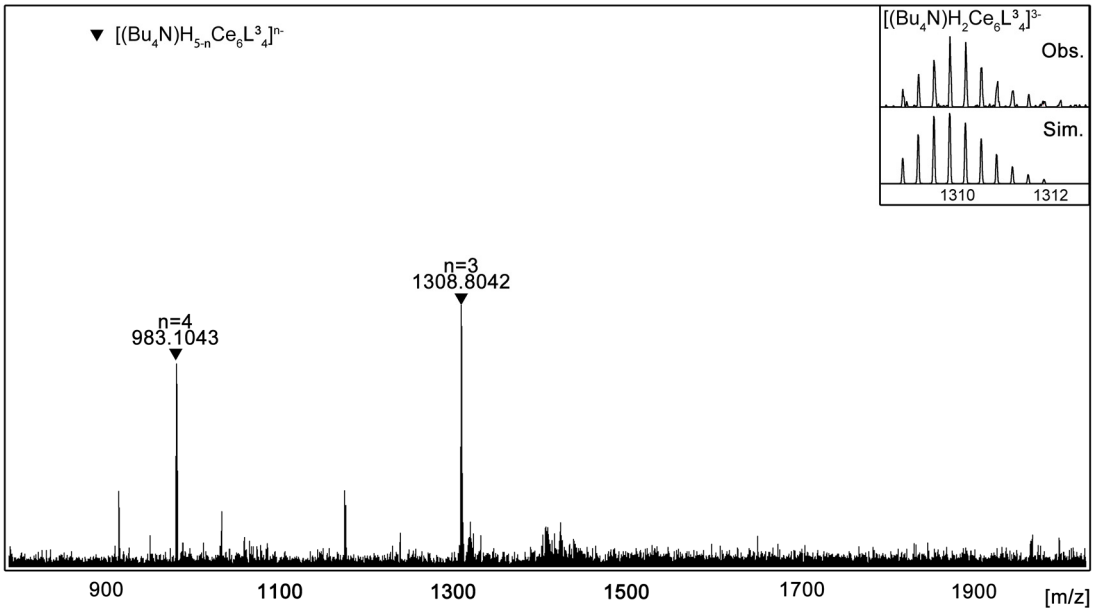

Figure S30 ESI-TOF-MS of $(Bu_4N)_6Ce_6\mathbf{L}^3_4$ with the observed and simulated isotopic patterns of the peaks corresponding to $[(Bu_4N)H_2Ce_6\mathbf{L}^3_4]^{3-}$.

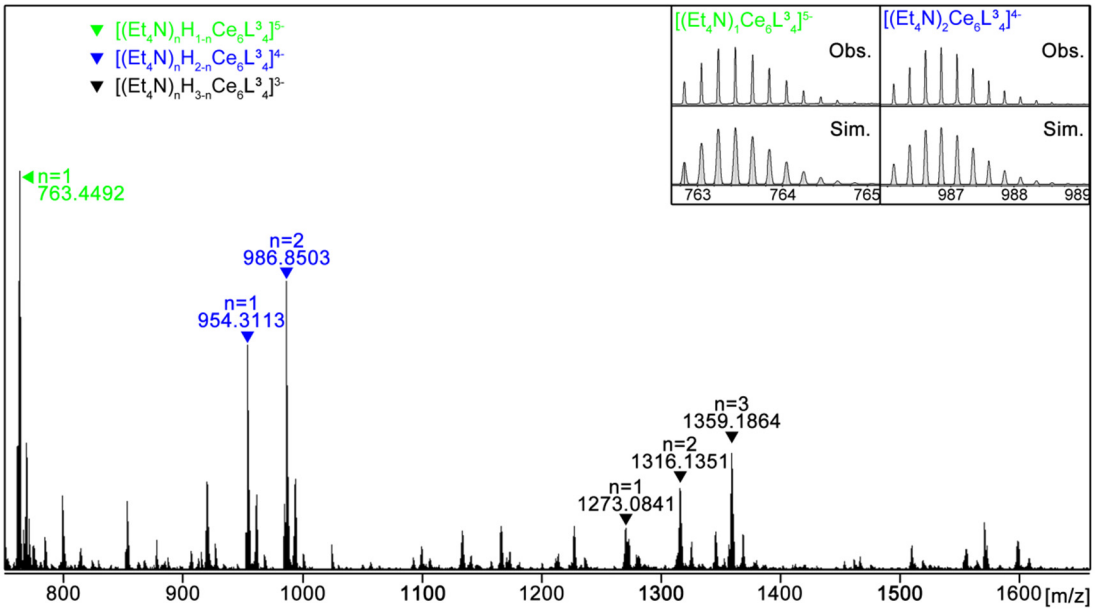

Figure S31 ESI-TOF-MS of Δ_6/Λ_6-$(Et_4N)_6Ce_6\mathbf{L}^3_4$ with the observed and simulated isotopic patterns of the peaks corresponding to $[(Et_4N)_1Ce_6\mathbf{L}^3_4]^{5-}$ and $[(Et_4N)_2Ce_6\mathbf{L}^3_4]^{4-}$, respectively.

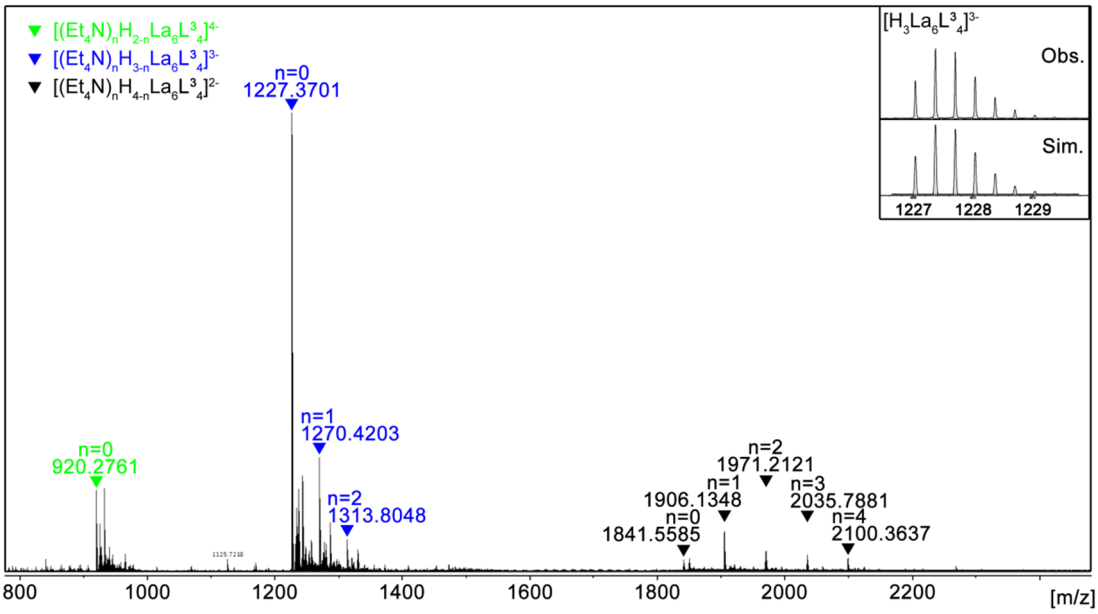

Figure S32 ESI-TOF-MS of Δ_6/Λ_6-$(Et_4N)_6La_6\mathbf{L^3}_4$ with the observed and simulated isotopic patterns of the peak corresponding to $[H_3La_6\mathbf{L^3}_4]^{3-}$.

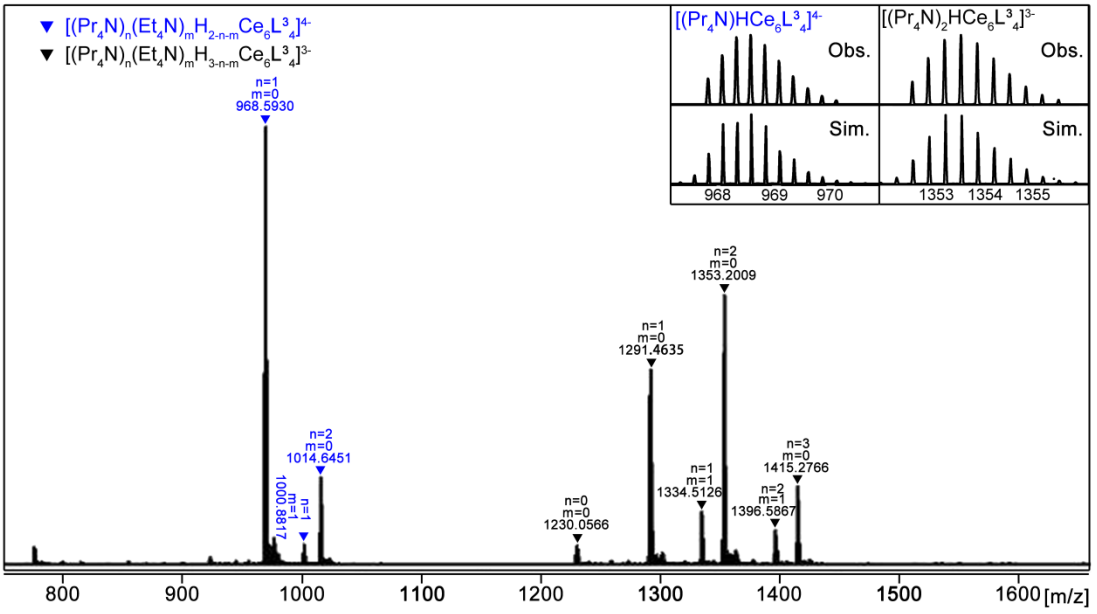

Figure S33 ESI-TOF-MS of adding 45 equiv. $Pr_4N{\cdot}Br$ into Δ_6/Λ_6-$(Et_4N)_6Ce_6\mathbf{L^3}_4$ with the observed and simulated isotopic patterns of the peak corresponding to $[(Pr_4N)_1HCe_6\mathbf{L^3}_4]^{4-}$ and $[(Pr_4N)_2HCe_6\mathbf{L^3}_4]^{3-}$.

3. Single crystal X-ray diffraction studies

High quality red single crystals of $La_4(H_3\mathbf{L^3})_2(OTf)_6$ suitable for crystallographic analysis were obtained by the slow vapor diffusion of chloroform vapor into the assembly solution of $H_6\mathbf{L^3}$ and $La(OTf)_3$ ([$H_6\mathbf{L^3}$]:La = 2:4) in acetonitrile/methanol (v/v=1:1) over one week.

High quality red single crystals of $Eu_4(H_3\mathbf{L^3})_2(OTf)_6$ suitable for crystallographic analysis were obtained by the slow vapor diffusion of diethyl ether vapor into the assembly solution of $H_6\mathbf{L^3}$ and $Eu(OTf)_3$ ([$H_6\mathbf{L^3}$]:Eu = 2:4) in acetonitrile/methanol (v/v=1:1) over one week.

High quality red single crystals of $Eu_6(H_3\mathbf{L^{3'}})_6(OTf)_6$ suitable for crystallographic analysis were obtained by the slow vapor diffusion of diethyl ether vapor into the assembly solution of $H_6\mathbf{L^3}$ and $Eu(OTf)_3$ ([$H_6\mathbf{L^3}$]:Eu = 2:3) in acetonitrile/methanol (v/v=1:1) over one week.

High quality red single crystals of Δ_6/Λ_6-$(Et_4N)_6Ce_6\mathbf{L^3}_4$ for crystallographic analysis were obtained by the slow vapor diffusion of tetrahydrofuran vapor into the DMSO/CH_3OH/CH_3CN (v/v/v=1:1:1) solution of Δ_6/Λ_6-$(Et_4N)_6Ce_6\mathbf{L^3}_4$ after two weeks.

The X-ray diffraction studies for complexes were carried out on Bruker D8 VENTURE photon II diffractometer with Iμs 3.0 microfocus X-ray source using APEX III program.[S2] Data reduction was performed with the SAINT and SADABS package. Both structures were solved by direct methods and refined by full-matrix least-squares on F2 with anisotropic displacement using the SHELX software package.[S3] Solvent molecules were highly disordered and could not be reasonably located. These residual intensities were removed by PLATON/SQUEEZE routine.[S4]

Crystal data for $La_4(H_3\mathbf{L^3})_2(OTf)_6$ (CCDC-2526860): Space group *P-1*, a = 8.44880(10) Å, b = 21.1975(3) Å, c = 24.5357(3) Å, α = 65.2720(10)°, β = 84.4650(10)°, γ = 81.5820(10)°, V = 3945.22(9) $Å^3$, Z = 1, T = 100(2) K. Anisotropic least-squares refinement for the framework atoms and isotropic refinement for the other atoms on 27880 independent merged reflections (*Rint*= 0.0261) converged at residual *wR2* = 0.2798 for all data; residual *R1* = 0.1183 for 7595 observed data [$I > 2\sigma(I)$], and

goodness of fit (GOF) = 1.121.

Crystal data for $Eu_4(H_3\mathbf{L^3})_2(OTf)_6$ (CCDC-2526858): Space group *P-1*, a = 8.4599(14) Å, b = 21.193(3) Å, c = 24.178(4) Å, α = 64.997(5)°, β = 84.082(6)°, γ = 80.960(5)°, V = 3876.7(11) $Å^3$, Z = 1, T = 150(2) K. Anisotropic least-squares refinement for the framework atoms and isotropic refinement for the other atoms on 29521 independent merged reflections (*Rint*= 0.0930) converged at residual *wR2* = 0.3316 for all data; residual *R1* =0.1247 for 6503 observed data [$I > 2\sigma(I)$], and goodness of fit (GOF) = 1.011.

Crystal data for $Eu_6(H_2\mathbf{L^{3'}})_6(OTf)_6$ (CCDC-2526859): Space group *R-3*, a = 36.839(3) Å, b = 36.839(3) Å, c = 37.075(4) Å, α = 90°, β = 90°, γ = 120°, V = 43573(9) $Å^3$, Z = 6, T = 104(2) K. Anisotropic least-squares refinement for the framework atoms and isotropic refinement for the other atoms on 13928 independent merged reflections (*Rint*= 0.0790) converged at residual *wR2* = 0.5164for all data; residual *R1* = 0.1741 for 7484 observed data [$I > 2\sigma(I)$], and goodness of fit (GOF) = 1.798.

Crystal data for Δ_6/Λ_6-$(Et_4N)_6Ce_6\mathbf{L^3}_4$ (CCDC-2526857): Space group *C2/c*, a = 40.3064(8) Å, b = 25.8476(3) Å, c = 32.2195(4) Å, α = 90°, β = 124.060(2)°, γ = 90°, V = 27808.6(9) $Å^3$, Z = 4, T = 100(2) K. Anisotropic least-squares refinement for the framework atoms and isotropic refinement for the other atoms on 38587 independent merged reflections (*Rint*= 0.0468) converged at residual *wR2* = 0.2034 for all data; residual *R1* = 0.0738 for 6555 observed data [$I > 2\sigma(I)$], and goodness of fit (GOF) = 1.044.

Table S2 Crystal data and structure refinement for $La_4(H_2\mathbf{L}^3)_2(OTf)_6$.

Identification code	$La_4(H_2\mathbf{L}^3)_2(OTf)_6$	
Empirical formula	C92 H70 F30 La4 N18 O52 S10	
Formula weight	3705.90	
Temperature	100(2) K	
Wavelength	0.71073 Å	
Crystal system	Triclinic	
Space group	P-1	
Unit cell dimensions	a = 8.44820(10) Å	α = 65.2720(10) Å
	b = 21.1951(3) Å	β = 84.4650(10) Å
	c = 24.5357(3) Å	γ = 81.5820(10) Å
Volume	3943.34(9) $Å^3$	
Z	1	
Density (calculated)	1.560 Mg/m^3	
Absorption coefficient	1.308 mm^{-1}	
F(000)	1822	
Crystal size	0.6 x 0.4 x 0.08 mm^3	
Theta range for data collection	1.829 to 20.389° .	
Index ranges	-8<=h<=8, -20<=k<=20, -24<=l<=24	
Reflections collected	27880	
Independent reflections	7782 [R(int) = 0.0261]	
Completeness to theta = 20.389°	99.9 %	
Absorption correction	Semi-empirical from equivalents	
Max. and min. transmission	1.00000 and 0.60675	
Refinement method	Full-matrix least-squares on F^2	
Data / restraints / parameters	7782 / 907 / 906	
Goodness-of-fit on F^2	1.121	
Final R indices [I>2sigma(I)]	R1 = 0.1183, wR2 = 0.2791	
R indices (all data)	R1 = 0.1196, wR2 = 0.2798	
Extinction coefficient	n/a	
Largest diff. peak and hole	2.428 and -2.435 e.$Å^{-3}$	

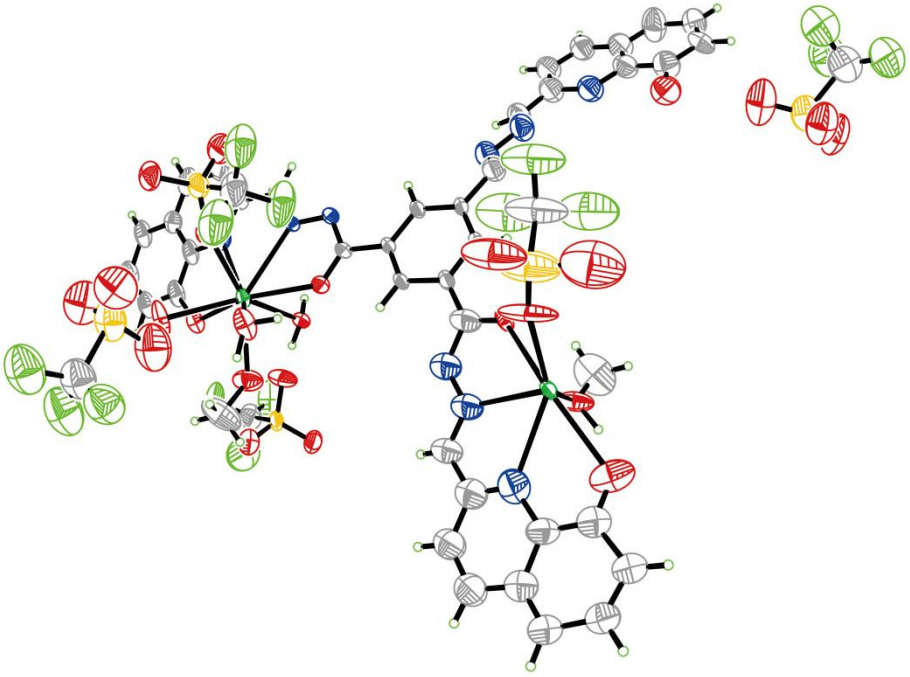

Figure S34 Ortep drawing of the asymmetric unit in the crystal structure of $La_4(H_2\mathbf{L}^3)_2(OTf)_6$ at 30% probability level.

Table S3 Crystal data and structure refinement for $Eu_4(H_2\mathbf{L}^3)_2(OTf)_6$.

Identification code	$Eu_4(H_2\mathbf{L}^3)_2(OTf)_6$	
Empirical formula	C92 H70 Eu4 F30 N18 O52 S10	
Formula weight	3758.10	
Temperature	150(2) K	
Wavelength	0.71073 Å	
Crystal system	Triclinic	
Space group	P-1	
Unit cell dimensions	a = 8.4599(14) Å	α = 64.997(5)°.
	b = 21.193(3) Å	β = 84.082(6)°.
	c = 24.178(4) Å	γ = 80.960(5)°.
Volume	3876.7(11) $Å^3$	
Z	1	
Density (calculated)	1.610 Mg/m^3	
Absorption coefficient	1.847 mm^{-1}	
F(000)	1846	
Crystal size	0.15 x 0.06 x 0.06 mm3	
Theta range for data collection	2.440 to 21.947°.	
Index ranges	-8<=h<=8, -22<=k<=22, -23<=l<=25	
Reflections collected	29521	
Independent reflections	9322 [R(int) = 0.0930]	
Completeness to theta = 21.948°	98.7 %	
Absorption correction	None	
Refinement method	Full-matrix least-squares on F^2	
Data / restraints / parameters	9322 / 1090 / 881	
Goodness-of-fit on F^2	1.011	
Final R indices [I>2sigma(I)]	R1 = 0.1247, wR2 = 0.3069	
R indices (all data)	R1 = 0.1592, wR2 = 0.3316	
Extinction coefficient	n/a	
Largest diff. peak and hole	2.259 and -1.694 e.$Å^{-3}$	

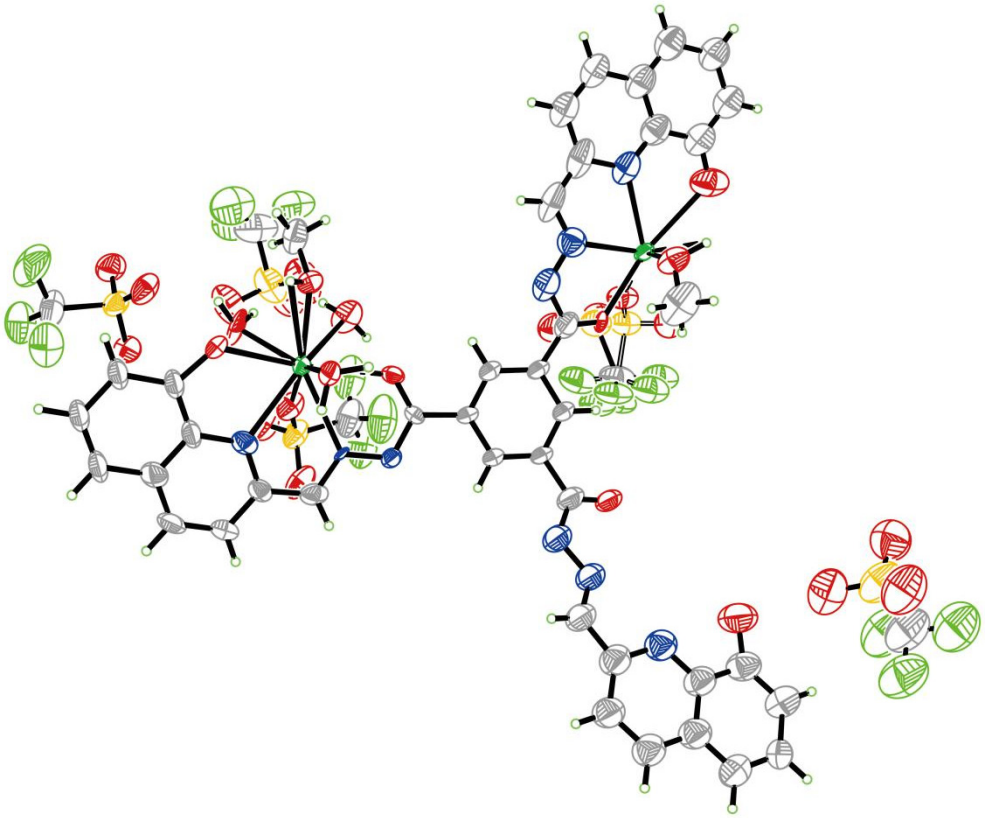

Figure S35 Ortep drawing of the asymmetric unit in the crystal structure of $Eu_4(H_2\mathbf{L}^3)_2(OTf)_6$ at 30% probability level.

Table S4 Crystal data and structure refinement for $Eu_6(H_2\mathbf{L^{3'}})_6(OTf)_6$.

Identification code	$Eu_6(H_2\mathbf{L^{3'}})_6(OTf)_6$	
Empirical formula	C180 H132 Eu6 F9 N48 O48 S3	
Formula weight	4917.29	
Temperature	104(2) K	
Wavelength	0.71073 Å	
Crystal system	Trigonal	
Space group	R-3	
Unit cell dimensions	a = 36.839(3) Å	α = 90°.
	b = 36.839(3) Å	β = 90°.
	c = 37.075(4) Å	γ = 120°.
Volume	43573(9) $Å^3$	
Z	6	
Density (calculated)	1.124 Mg/m^3	
Absorption coefficient	1.365 mm^{-1}	
F(000)	14652	
Crystal size	0.072 x 0.068 x 0.065 mm^3	
Theta range for data collection	2.211 to 23.280°.	
Index ranges	-40<=h<=40, -39<=k<=39, -40<=l<=41	
Reflections collected	61952	
Independent reflections	13928 [R(int) = 0.0790]	
Completeness to theta = 23.280°	99.7 %	
Absorption correction	None	
Refinement method	Full-matrix least-squares on F^2	
Data / restraints / parameters	13930 / 711 / 765	
Goodness-of-fit on F^2	1.780	
Final R indices [I>2sigma(I)]	R1 = 0.1741, wR2 = 0.4666	
R indices (all data)	R1 = 0.2428, wR2 = 0.5164	
Extinction coefficient	n/a	
Largest diff. peak and hole	2.012 and -1.325 e.Å-3	

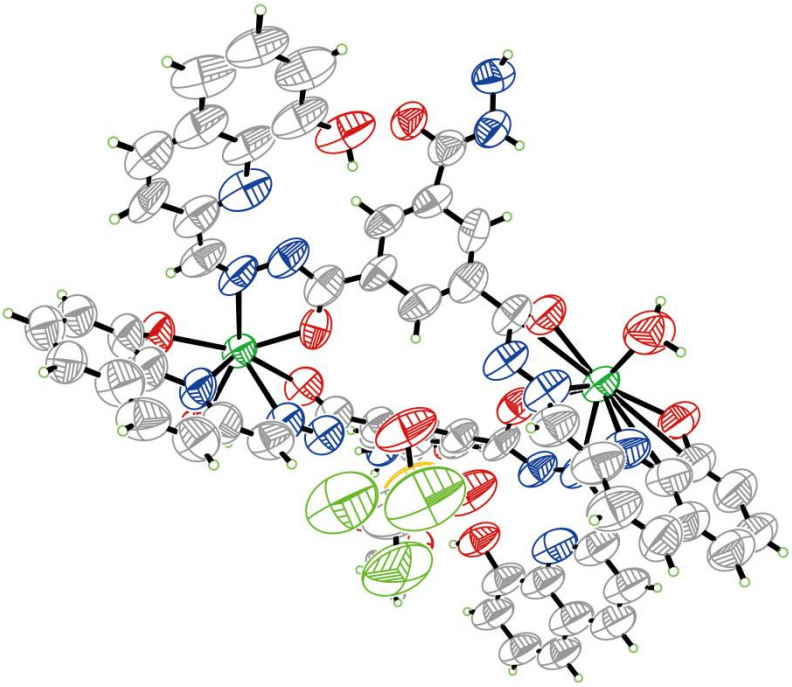

Figure S36 Ortep drawing of the asymmetric unit in the crystal structure of $Eu_6(H_2\mathbf{L}^{3'})_6(OTf)_6$ at 30% probability level.

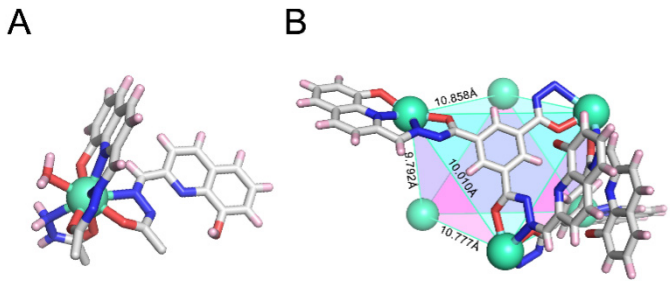

Figure S37 (A) the coordination geometry on the Eu center; (B) the abstract graph of the anti-triangular prism structure of $Eu_6(H_3\mathbf{L}^{3'})_6(OTf)_6$.

Weak interaction analysis: Independent gradient model (IGM) analysis[S5] was performed using Multiwfn 3.8[S6] to investigate the inter-ligand weak interactions, and the results were visualized with VMD 2.0.0[S7]. To quantify and visualize the supramolecular interactions in $Eu_6(H_3\mathbf{L}^{3'})_6$, a Hirshfeld surface analysis was carried out with CrystalExplorer17[S8]. The Hirshfeld surface and fingerprint plots for $Eu_6(H_3\mathbf{L}^{3'})_6$ are shown in Figure S39, and the percentage contributions of the various contacts are summarized in Figure S40. Intermolecular H···H contacts dominate, accounting for 50.6%, while π–π interactions (C···C contacts) are present at 2.4%.

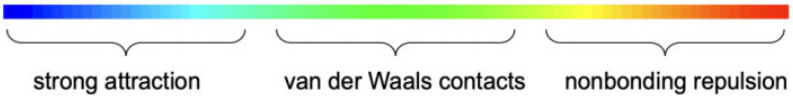

Figure S38. Color-coded sign scale bar of IGM analysis.

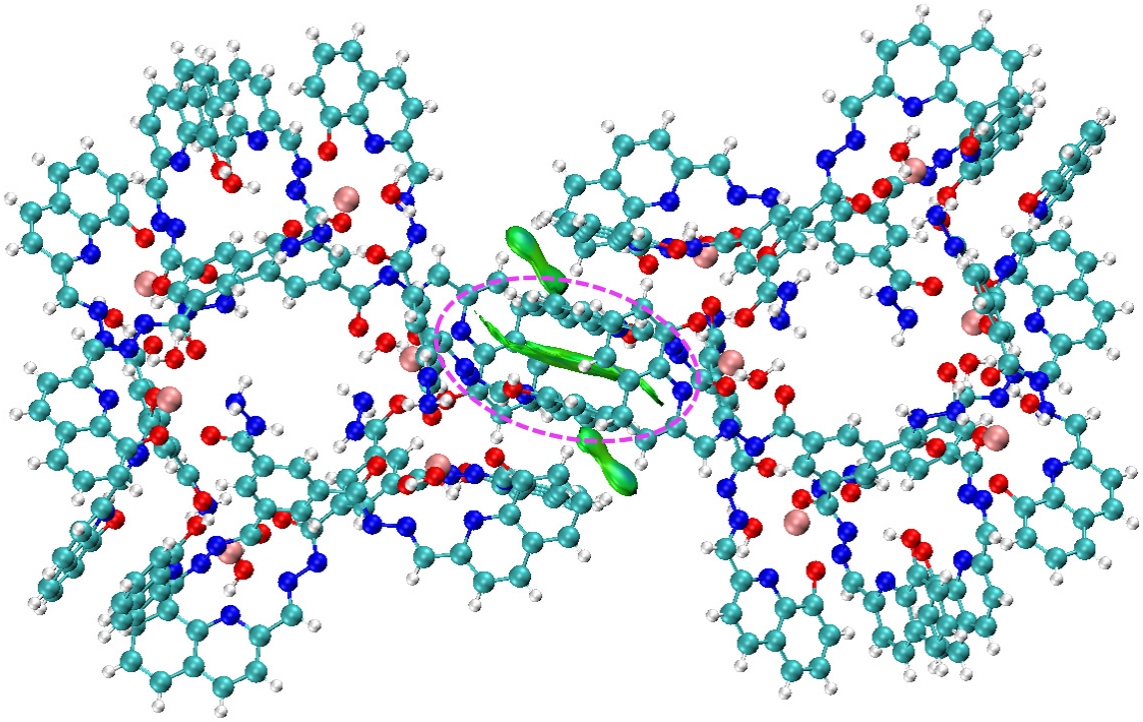

Figure S39. IGM analysis of $Eu_6(H_3\mathbf{L}^{3'})_6(OTf)_6$ complex (δginter = 0.005).

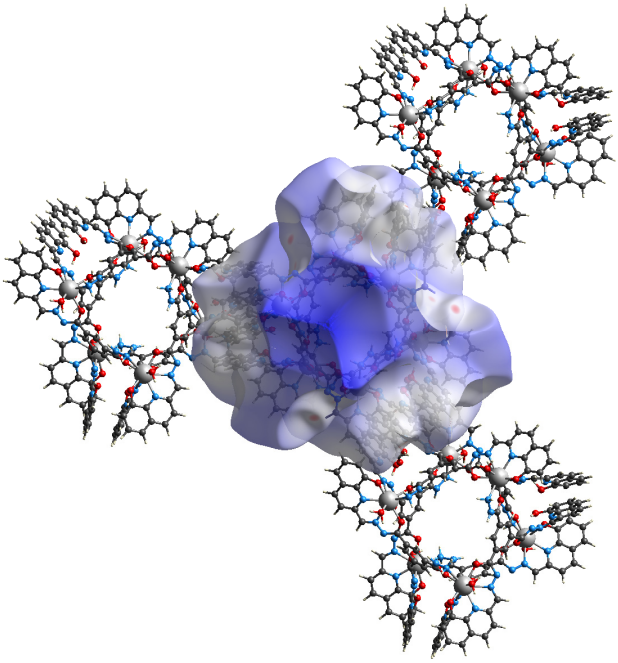

Figure S40 Hirshfeld surfaces of $Eu_6(H_3\mathbf{L}^{3'})_6(OTf)_6$.

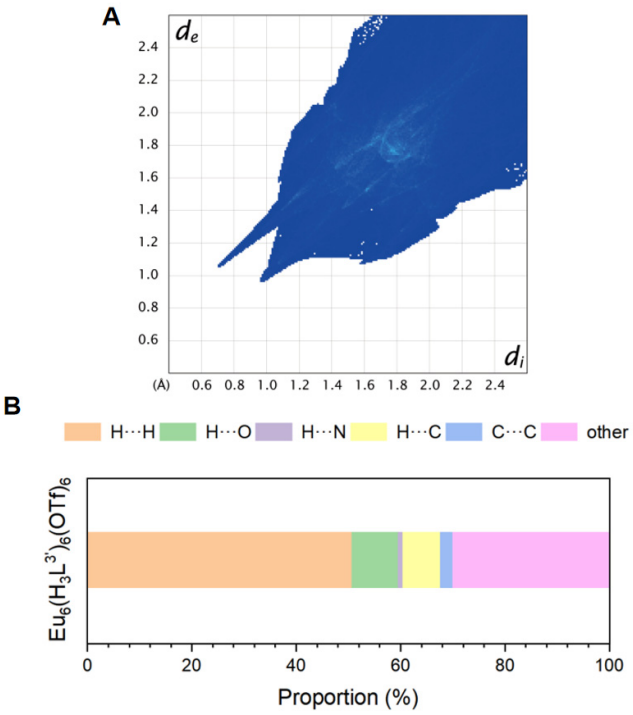

Figure S41 (A) 2D fingerprint plots for $Eu_6(H_3\mathbf{L}^{3'})_6(OTf)_6$; (B) Percentage contributions of the average interactions for $Eu_6(H_3\mathbf{L}^{3'})_6(OTf)_6$ (H···H 50.6%, H···O 8.9%, H···N 0.9%, H···C 7.2%, C···C 2.4%, other 30.0%).

Table S5 Crystal data and structure refinement for Δ_6/Λ_6-$(Et_4N)_6Ce_6\mathbf{L^3}_4$.

Identification code	Δ_6/Λ_6-$(Et_4N)_6Ce_6\mathbf{L^3}_4$	
Empirical formula	C164 H104 Ce6 N37 O24	
Formula weight	3817.56	
Temperature	100(2) K	
Wavelength	1.34139 Å	
Crystal system	Monoclinic	
Space group	C2/c	
Unit cell dimensions	a = 40.3064(8) Å	α = 90°
	b = 25.8476(3) Å	β = 124.060(2)°
	c = 32.2195(4) Å	γ = 90°
Volume	27808.6(9) $Å^3$	
Z	4	
Density (calculated)	0.912 Mg/m^3	
Absorption coefficient	5.370 mm^{-1}	
F(000)	7548	
Crystal size	0.16 x 0.09 x 0.026 mm^3	
Theta range for data collection	2.484 to 33.975°	
Index ranges	-33<=h<=30, -21<=k<=21, -23<=l<=26	
Reflections collected	38587	
Independent reflections	8390 [R(int) = 0.0468]	
Completeness to theta = 33.975?	99.5 %	
Absorption correction	Semi-empirical from equivalents	
Max. and min. transmission	1.00000 and 0.83150	
Refinement method	Full-matrix least-squares on F^2	
Data / restraints / parameters	8390 / 426 / 875	
Goodness-of-fit on F^2	1.044	
Final R indices [I>2sigma(I)]	R1 = 0.0738, wR2 = 0.1891	
R indices (all data)	R1 = 0.0910, wR2 = 0.2034	
Extinction coefficient	n/a	
Largest diff. peak and hole	0.897 and -0.360 $e.Å^{-3}$	

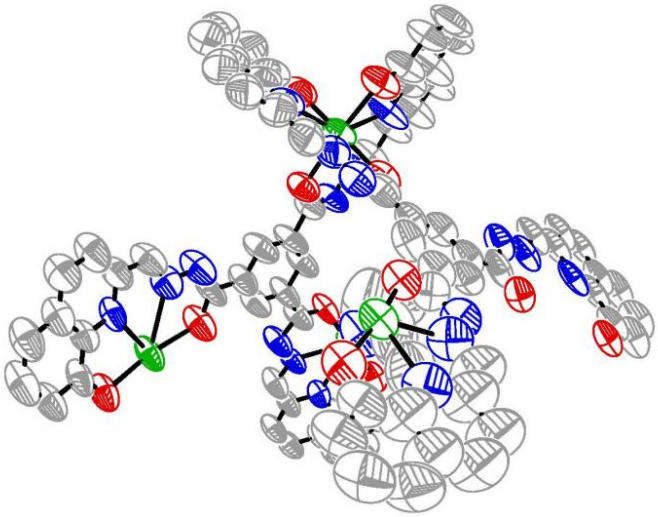

Figure S42 Ortep drawing of the asymmetric unit in the crystal structure of Δ_6/Λ_6-$(Et_4N)_6Ce_6\mathbf{L}^3{}_4$ at 30% probability level.

MoloVol[3] calculations based on the crystal structures of Δ_6/Λ_6-$(Et_4N)_6Ce_6\mathbf{L}_4$ and Δ_6/Λ_6-$(Et_4N)_6Yb_6\mathbf{L}_4$ were performed with anions, disorder and solvent molecules removed to determine the available void spaces of their host cavties. A probe with a radius of 2.3 Å was employed in all cases. The standard parameters are tabulated below, and the results are shown in Figure S34.

Probe mode: one probe
Probe radius: 2.3 Å
Grid resolution: 0.2 Å
Optimization depth: 4

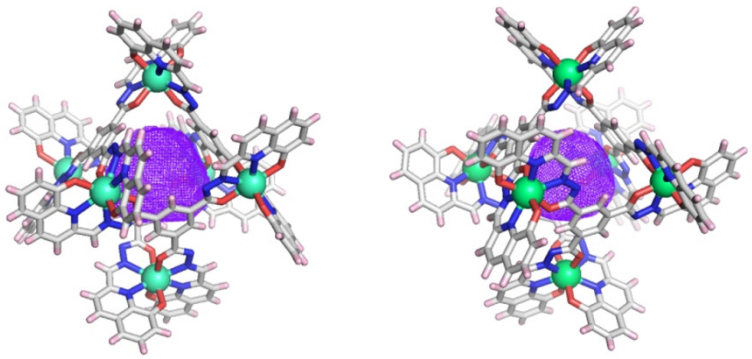

Figure S43 MoloVol[3] -calculated void space (purple mesh) within the crystal structures of Δ_6/Λ_6-$(Et_4N)_6Ce_6\mathbf{L}_4$ and Δ_6/Λ_6-$(Et_4N)_6Yb_6\mathbf{L}_4$.

4. The Host-Guest Chemistry.

First, 1,3,5-trimethoxybenzene as an interior standard was added into the solution of Δ_6/Λ_6-$(Et_4N)_6Ce_6\mathbf{L^3}_4$ (G_1: Et_4N^+) to determine the concentration of the host. The ^1H NMR titration was carried out at room temperature. In the titration, small aliquots of the guest $Pr_4N{\cdot}Br$ (G_2: Pr_4N^+) were added to a 500 μL of Δ_6/Λ_6-$(Et_4N)_6Ce_6\mathbf{L^3}_4$ with 1,3,5-trimethoxybenzene (0.25 mg/ml) as an internal standard in *d*$_6$-DMSO. The total host and guest concentrations were determined based on the internal standard. The relative binding constant were determined according to Eq. 1. [S9]

$$[HG_2] = \frac{\left[\frac{K_2}{K_1}([G_2]_0+[H]_0)+([G_1]_0-[H]_0)\right]-\sqrt{\left[\frac{K_2}{K_1}([G_2]_0+[H]_0)+([G_1]_0-[H]_0)\right]^2-4(\frac{K_2}{K_1}-1)\frac{K_2}{K_1}[G_2]_0[H]_0}}{2(\frac{K_2}{K_1}-1)} \qquad \text{Eq. 1}$$

using origin to fit the binding data,

$$Y=((B*(X+P)+(R-P))-\text{sqrt}(((B*(X+P)+(R-P))\text{^}2)-4*(B-1)*(B*X*P))/(2*(B-1)) \qquad \text{Eq. 2}$$

Y Concentration of Host-Guest2 complex = $[HG_2]$
B Ratio of the two binding constants = K_2 / K_1
P Total host concentration ($[H]_0$)
R Total Guest1 concentration = $[G_1]_0$
X Total Guest2 concentration = $[G2]_0$

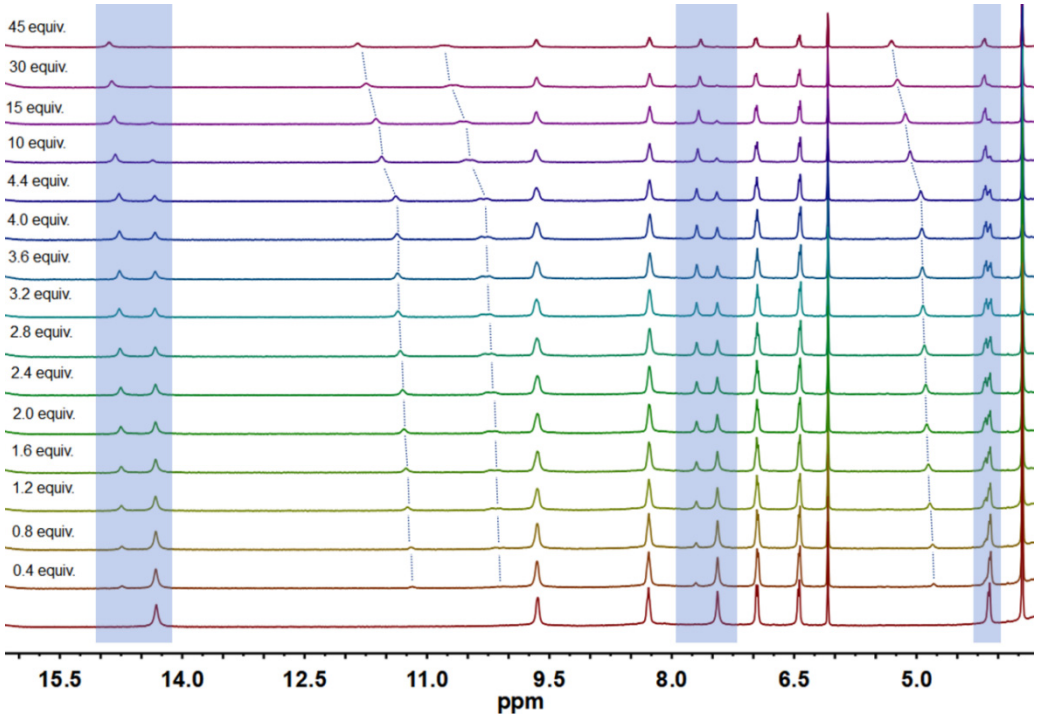

Figure S44 ^1H NMR (400 MHz, *d*$_6$-DMSO, 298 K) titration of Δ_6/Λ_6-$(Et_4N)_6Ce_6\mathbf{L^3}_4$ with $Pr_4N{\cdot}Br$.

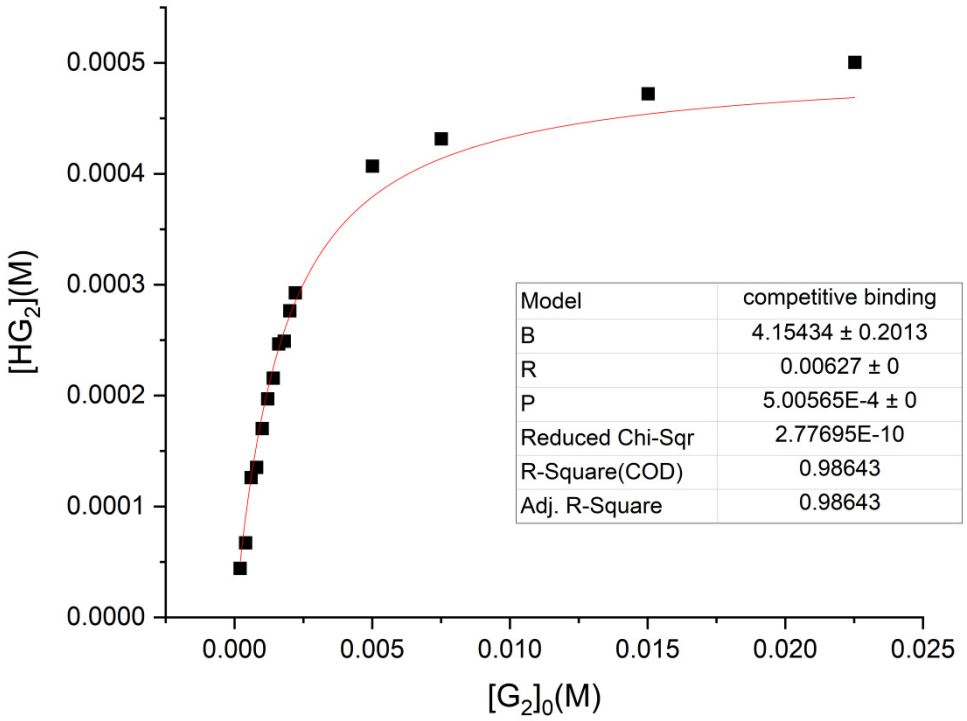

Figure S45 Data fitting for the titration of the slow exchanging Pr_4N^+ guest into a solution of Δ_6/Λ_6-$(Et_4N)_6Ce_6\mathbf{L}^3{}_4$. A competitive binding constant K_2/K_1 of 4.15 was determined for Pr_4N^+ into Δ_6/Λ_6-$(Et_4N)_6Ce_6\mathbf{L}^3{}_4$.

We also carried out the competition experiments by adding 9.0 equiv. of guests ($Me_4N\cdot Br$ and $Bu_4N\cdot Br$) to a solution of Δ_6/Λ_6-$(Et_4N)_6Ce_6\mathbf{L}^3{}_4$ to examine the size selectivity. Addition of Me_4N^+ produced no significant shift in the ^{1}H NMR of Δ_6/Λ_6-$Ce_6\mathbf{L}^3{}_4$, indicating weaker host-guest interaction with Me_4N^+ than with Et_4N^+. In contrast, similar to the case of Pr_4N^+, addition of $Bu_4N\cdot Br$ gave new signals assignable to the protons of $Bu_4N^+\subset Ce_6\mathbf{L}^3{}_4$. The relative binding constant $K(Bu_4N^+)/K(Et_4N^+)$ was calculated to be 0.26. Thus, the binding abilities of Δ_6/Λ_6-$Ce_6\mathbf{L}^3{}_4$ toward these four ammoniums follow the sequence of $Me_4N^+ < Bu_4N^+ < Et_4N^+ < Pr_4N^+$.

Analogous competition experiments were also conducted with Δ_6/Λ_6-$(Et_4N)_6La_6\mathbf{L}^3{}_4$. Interestingly, the binding abilities of Δ_6/Λ_6-$La_6\mathbf{L}^3{}_4$ follow a different sequence: $Me_4N^+ < Et_4N^+ < Pr_4N^+ < Bu_4N^+$, with Δ_6/Λ_6-$La_6\mathbf{L}^3{}_4$ showing the strongest encapsulation of Bu_4N^+. These results suggest that a larger lanthanide ionic radius can expand the cavity of the tetra-capped octahedron, resulting in a stronger encapsulation toward lager alkylammonium cation.

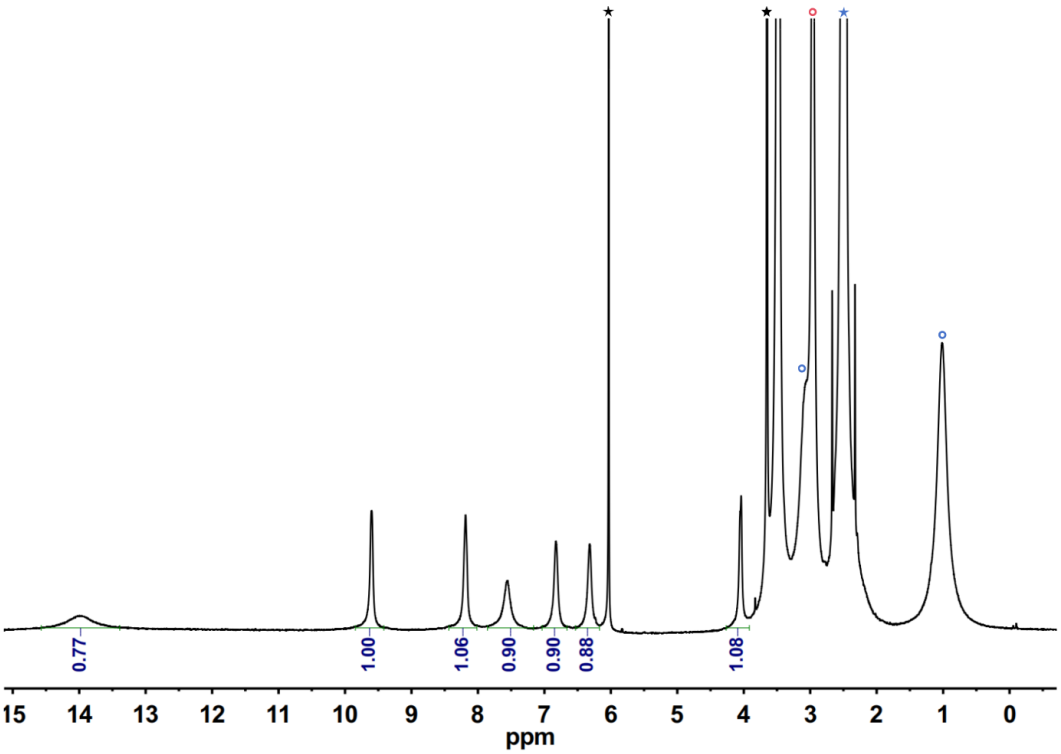

Figure S46 ^{1}H NMR spectrum of Δ_6/Λ_6-$(Et_4N)_6Ce_6\mathbf{L^3}_4$ after the addition of 9.0 equiv. of $Me_4N{\cdot}Br$. (400 MHz, d_6-DMSO, 298 K, ★: the interior standard of 1,3,5-trimethoxybenzene, ★: DMSO, ○: free Me_4N^+, ○: free Et_4N^+).

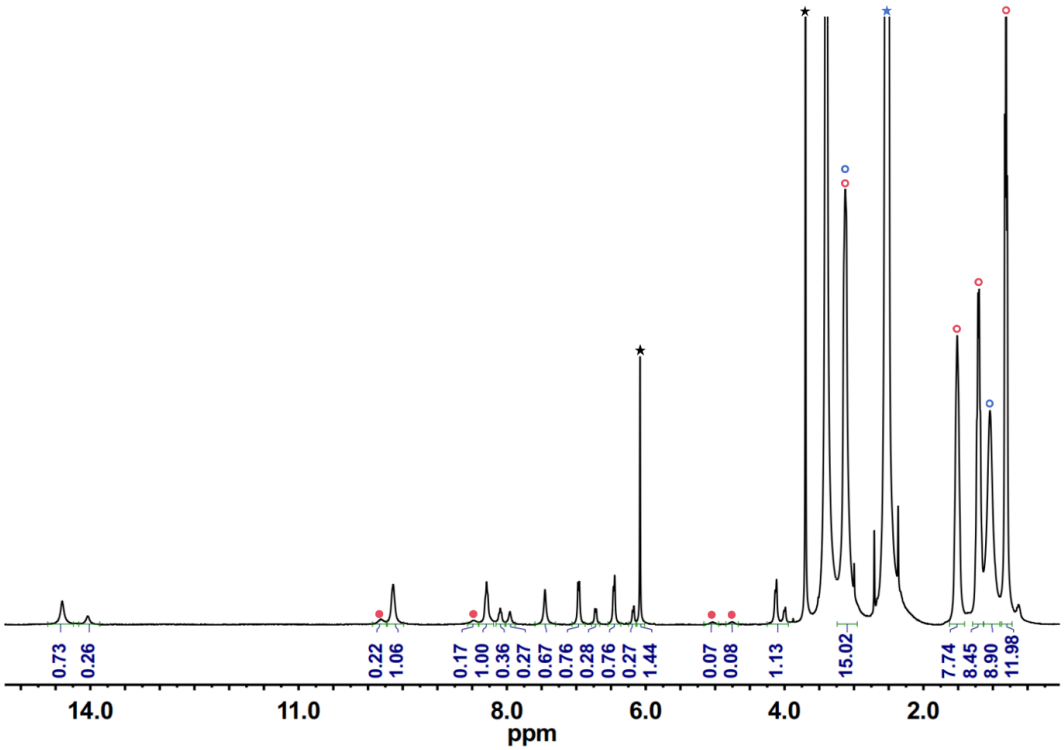

Figure S47 ^{1}H NMR spectrum of Δ_6/Λ_6-$(Et_4N)_6Ce_6\mathbf{L^3}_4$ after the addition of 9.0 equiv. of $Bu_4N{\cdot}Br$. (400 MHz, d_6-DMSO, 298 K, ★: the interior standard of 1,3,5-trimethoxybenzene, ★: DMSO, ●: encapsulated Bu_4N^+, ○: free Bu_4N^+, ○: free Et_4N^+). A relative binding constant $K(Pr_4N^+)/K(Et_4N^+)$ of 0.27 was determined.

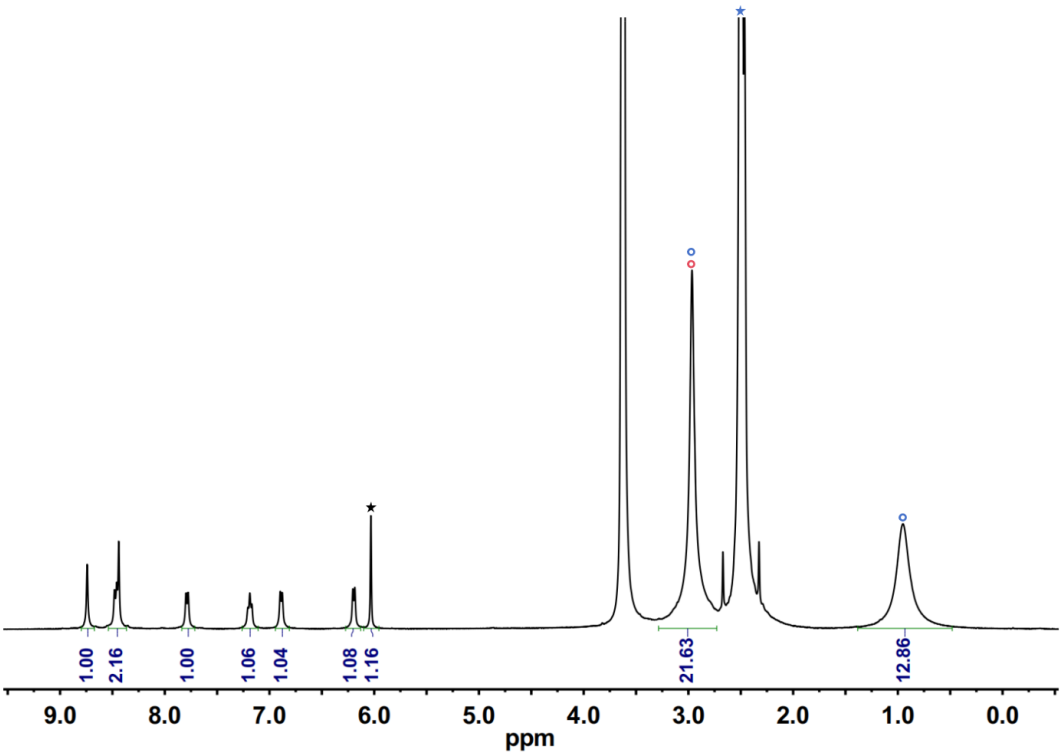

Figure S48 ^{1}H NMR spectrum of Δ_6/Λ_6-$(Et_4N)_6La_6\mathbf{L}^3{}_4$ after the addition of 9.0 equiv. of $Me_4N{\cdot}Br$. (400 MHz, d_6-DMSO, 298 K, ★: the interior standard of 1,3,5-trimethoxybenzene, ★: DMSO, ○: free Me_4N^+, ○: free Et_4N^+).

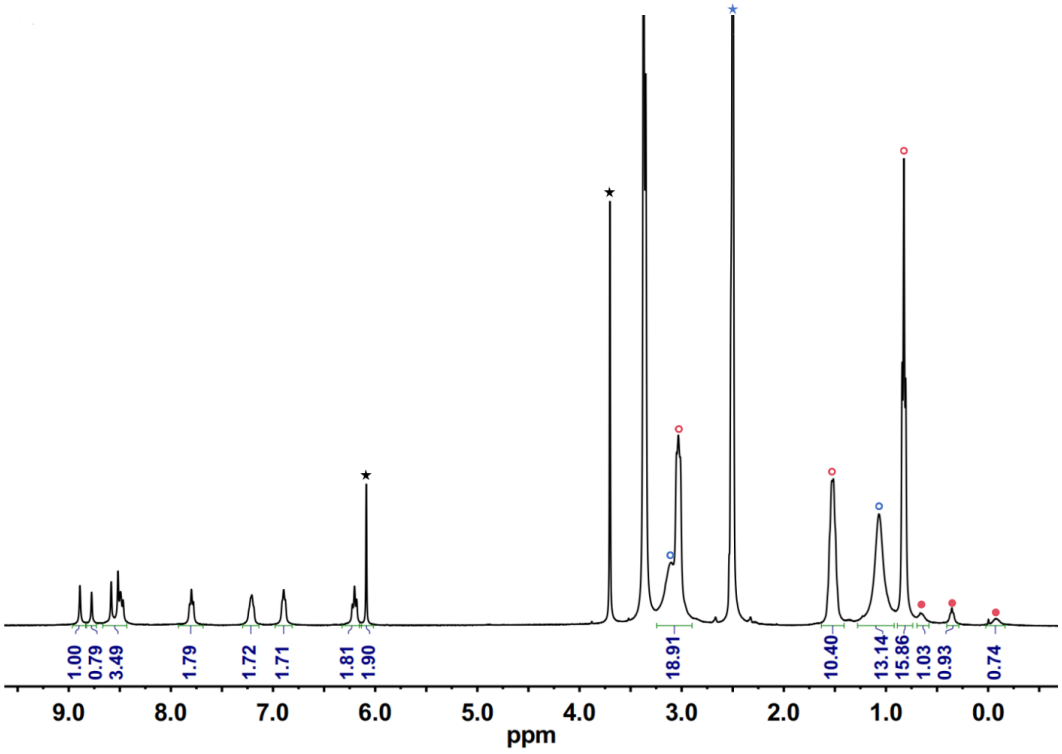

Figure S49 ^{1}H NMR spectrum of Δ_6/Λ_6-$(Et_4N)_6La_6\mathbf{L}^3{}_4$ after the addition of 9.0 equiv. of $Pr_4N{\cdot}Br$. (400 MHz, d_6-DMSO, 298 K, ★: the interior standard of 1,3,5-trimethoxybenzene, ★: DMSO, ●: encapsulated Pr_4N^+, ○: free Pr_4N^+, ○: free Et_4N^+). A relative binding constant $K(Pr_4N^+)/K(Et_4N^+)$ of 1.05 was determined.

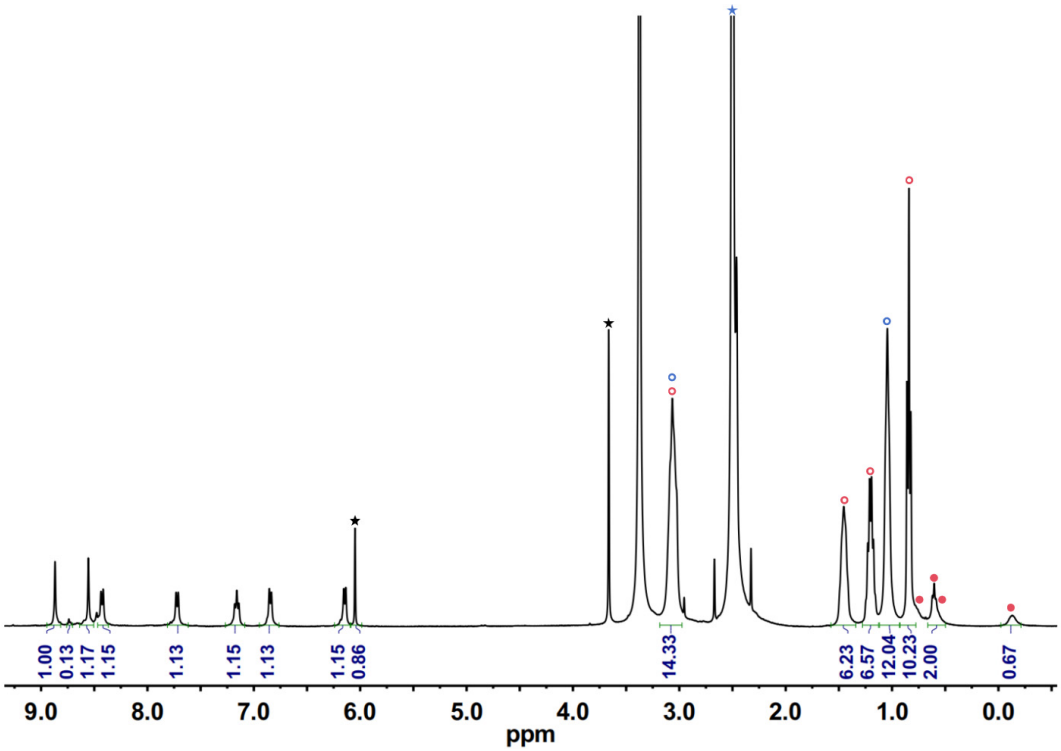

Figure S50 ^{1}H NMR spectrum of Δ_6/Λ_6-$(Et_4N)_6La_6\mathbf{L^3}_4$ after the addition of 9.0 equiv. of $Bu_4N{\cdot}Br$. (400 MHz, d_6-DMSO, 298 K, ★: the interior standard of 1,3,5-trimethoxybenzene, ★: DMSO, ●: encapsulated Bu_4N^+, ○: free Bu_4N^+, ○: free Et_4N^+). A relative binding constant $K(Bu_4N^+)/K(Et_4N^+)$ of 9.05 was determined.

5. Lanthanide-directed Self-Assembly Studies.

Table S6 The coordination bond lengths of different coordination modes

	$Eu_4(H_3\mathbf{L^3})_2$	$Eu_2(H_2\mathbf{L^1})_2$	$Eu_6\mathbf{L^3}_4$	$La_4(H_3\mathbf{L^3})_2$
O_{amide}-Ln	2.585	2.594	2.347	2.648
N_{amide}-Ln	2.665	2.627	2.478	2.722
$N_{hydrazine}$-Ln	2.637	2.649	2.542	2.712
O_{phenol}-Ln	2.470	2.464	2.378	2.539
θ	48.36°	48.71°	89.07°	46.20°

Table S7 The coordination bond lengths of Ln-Assembly for different coordination modes under neutral conditions

	$La_4(H_3\mathbf{L^3})_2$	$Eu_4(H_3\mathbf{L^3})_2$	$Eu_2(H_2\mathbf{L^1})_2$	$Lu_6(H_3\mathbf{L^3})_4$
O_{amide}-Ln	2.648	2.585	2.594	2.277
N_{amide}-Ln	2.722	2.665	2.627	2.375

$N_{hydrazine}$-Ln	2.712	2.637	2.649	2.473
O_{phenol}-Ln	2.539	2.470	2.464	2.317
θ	46.20°	48.36°	48.71°	88.84°

Table S8 The coordination bond lengths of Ln-Assembly for different coordination modes under basic condition

	$(Et_4N)\subset Ce_6\mathbf{L}^3{}_4$	$(Et_4N)\subset Eu_6\mathbf{L}^3{}_4$	$(Et_4N)\subset Yb_6\mathbf{L}^3{}_4$
O_{amide}-Ln	2.415	2.347	2.270
N_{amide}-Ln	2.578	2.478	2.396
$N_{hydrazine}$-Ln	2.608	2.712	2.444
O_{phenol}-Ln	2.438	2.378	2.270
θ	87.89°	89.20°	88.37°

6. Reference

[S1]Zhou, L.-P.; Feng, X.-S.; Hu, S.-J.; Sun, Q.-F., Controlled Self-Assembly, Isomerism, and Guest Uptake/Release of Charge-Reversible Lanthanide–Organic Octahedral Cages. *J. Am. Chem. Soc.* **2023,** *145* (32), 17845-17855.

[S2]APEX III, Data collection software (version 2017.3).

[S3]G. M. Sheldrick, *Acta Crystallogr. Sect. A* **2008**, *64*, 112-122.

[S4]A. L. Spek, *J. Appl. Crystallogr.* **2003**, *36*, 7–13.

[S5]Lefebvre, C.; Rubez, G.; Khartabil, H.; Boisson, J.-C.; Contreras-García, J.; Hénon, E. Accurately extracting the signature of intermolecular interactions present in the NCI plot of the reduced density gradient versus electron density. *Phys.Chem.Chem.Phys.* **2017,** *19*, 17928-17936.

[S6]Lu, T.; Chen, F. Multiwfn: A multifunctional wavefunction analyzer. *J. Comput. Chem.* **2012,** *33*, 580-592.

[S7]Humphrey, W.; Dalke, A.; Schulten, K. VMD: Visual molecular dynamics. *J. Mol. Graphics* **1996,** *14*, 33-38.

[S8]Spackman, P. R.; Turner, M. J.; McKinnon, J. J.; Wolff, S. K.; Grimwood, D. J.; Jayatilaka, D.; Spackman, M. A. CrystalExplorer: a program for Hirshfeld surface analysis, visualization and quantitative analysis of molecular crystals. *J. Appl. Crystallogr.* **2021,** *54*, 1006-1011.

[S9]Hristova, Y. R.; Smulders, M. M. J.; Clegg, J. K.; Breiner, B.; Nitschke, J. R., Selective anion binding by a "Chameleon" capsule with a dynamically reconfigurable exterior. *Chem. Sci.* **2011,** *2*(4), 638-641.